A Triply Nested Ocean Model for Simulating the Kuroshio—Roles of Horizontal Resolution on JEBAR

XINYU GUO

Center for Marine Environmental Studies, Ehime University, Matsuyama, and Institute for Global Change Research, Yokohama, Japan

HISASHI HUKUDA AND YASUMASA MIYAZAWA

Institute for Global Change Research, Yokohama, Japan

TOSHIO YAMAGATA

Department of Earth and Planetary Science, Graduate School of Science, The University of Tokyo, Tokyo, and Institute for Global Change Research, Yokohama, Japan

(Manuscript received 1 October 2001, in final form 25 June 2002)

ABSTRACT

A triply nested ocean general circulation model was used to examine how the model horizontal resolution influences the Kuroshio in the East China Sea (ECS) and the sea level variability. As the model resolution increases from ½° to 1/18°, the path, current intensity, and vertical structure of the model Kuroshio and the variability of sea level become closer to observations. In general, the higher-resolution model improves the baroclinic as well as barotropic component of the Kuroshio and thus reproduces more realistic density and current fields. This improvement, in addition to better representation of topography, results in better reproduction of the interaction between baroclinicity and bottom topography, that is, JEBAR (joint effect of baroclinicity and bottom relief) in a high-resolution model. Modeling the Kuroshio in the ECS provides an ideal example of such improvement. In particular, the Kuroshio veering phenomenon at (30°N, 129°E) southwest of Kyushu is discussed, together with the seasonal meridional migration of the path. It is shown that JEBAR and advection of the geostrophic potential vorticity are two major contributions to the vorticity balance in this area. The summer intensification of JEBAR resulting from the intensified stratification yields a strong offshore volume transport across the shelf break, thereby leading to the southward shift of the veering latitude. In winter, the weakened JEBAR, combined with the increased wind stress curl, decreases the offshore volume transport in a considerable amount, explaining the northward shift of the veering latitude. The present reproduction of seasonal migration of the Kuroshio axis at 129°E is in good agreement with observation.

1. Introduction

The Kuroshio, one of the major western boundary currents, influences not only global ocean climate variations but also the regional climate system in East Asia. It originates in the northward branch of the bifurcated North Equatorial Current off the Philippine coast (Nitani 1972), enters the East China Sea (ECS) east of Taiwan, and flows northeastward along the continental slope in the ECS. After passing through Tokara Strait south of Kyushu, the Kuroshio intensifies its speed and continues to flow along the southern coast of Japan, where it shows the well-known bimodal paths: the straight path and the meandering path. Then, it leaves Honshu (the main island of Japan) off the Boso Peninsula and enters the deep Pacific Ocean as the Kuroshio Extension.

Up to now, studies of the Kuroshio using basin-scale ocean models have mainly focused on the variation of the volume transport (Greatbatch and Goulding 1990; Sekine and Kutsuwada 1994; Kubota et al. 1995; Kagimoto and Yamagata 1997). Because of the limitation in model resolution, only the work of Kagimoto and Yamagata (1997) paid attention to the vertical structure of the Kuroshio. Using a 1/3° Pacific Ocean model, Kagimoto and Yamagata (1997) emphasized the importance of high resolution in simulating the Kuroshio, particularly in capturing JEBAR (joint effect of baroclinicity and bottom relief). Recently, Smith et al. (2000) also showed the importance of high resolution in simulations of the Gulf Stream. Their Atlantic Ocean model with 1/10° resolution reproduced the sea level variability

Corresponding author address: Xinyu Guo, Center for Marine Environmental Studies, Ehime University, 3 Bunkyo-cho, Matsuyama 790-8577, Japan.
E-mail: guoxinyu@dpc.ehime-u.ac.jp

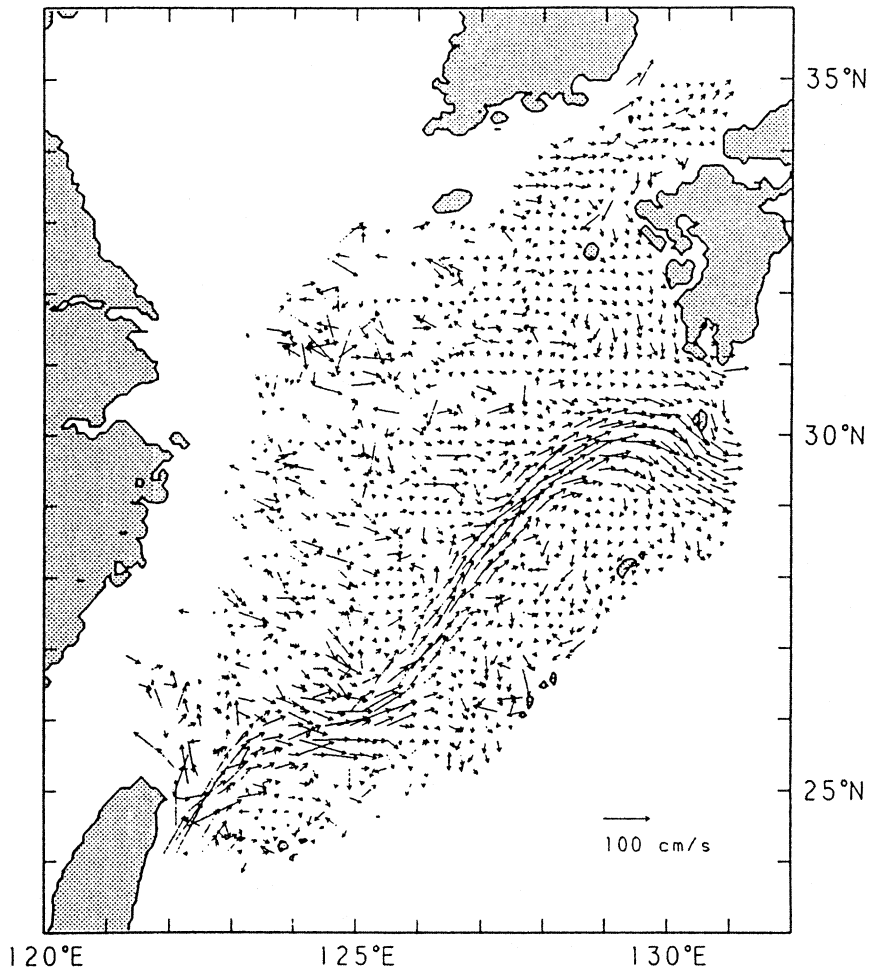

FIG. 1. Surface mean currents in the East China Sea derived from GEK data from 1953 to 1984 (after Qiu and Imasato 1990).

observed by the TOPEX/Poseidon altimeter, whereas their model with ⅕° resolution failed to do so.

The Kuroshio in the ECS is largely controlled by the bottom topography. For example, as shown by Qiu and Imasato (1990), the long-term GEK observation data (Fig. 1) demonstrate that the Kuroshio in the ECS approximately flows along the continental slope (see also Fig. 3 for the topography of ECS). However, there are at least two phenomena that cannot be explained by the topographic control. One is the Kuroshio around 30°N, 128°–129°E where it becomes free from the control of bottom topography and leaves the continental slope. This phenomenon is referred to as the Kuroshio veering. Another is the seasonal meridional migration of the Kuroshio path at 129°E (Sun and Su 1994). In this article, we will give an explanation of these two phenomena—that is, why the Kuroshio veers east at 30°N in the ECS and why the Kuroshio path shows the seasonal meridional migration at 129°E.

Since the continental slope in the ECS has a gradient of as much as 800 m in 20–30 km, a numerical model needs to have a grid size less than 10 km to resolve it. Also, we prefer a basin-scale model to a regional model to avoid the open boundary problem. To meet these two conflicting requirements, we adopt a one-way nested model. Figure 2 shows the three ocean models designed with a triply nested structure for the Pacific Ocean. These models, called NEST1, NEST2, NEST3, have grid sizes that decrease with a ratio of 1/3 in increasing order and are linked through their lateral interface where the coarser grid model results are used to specify the boundary conditions for the finer grid model. This way, we can satisfy the requirement of high resolution in the continental slope region and also circumvent the open boundary problem for the regional model. We did not adopt a two-way nested model in the present work because of complications that make it difficult to conserve some properties and because of excessive computer resources requirements.

In the next section, we give a brief description on the above three models, used for a hindcast experiment for the years 1992–98. In section 3, results of these models

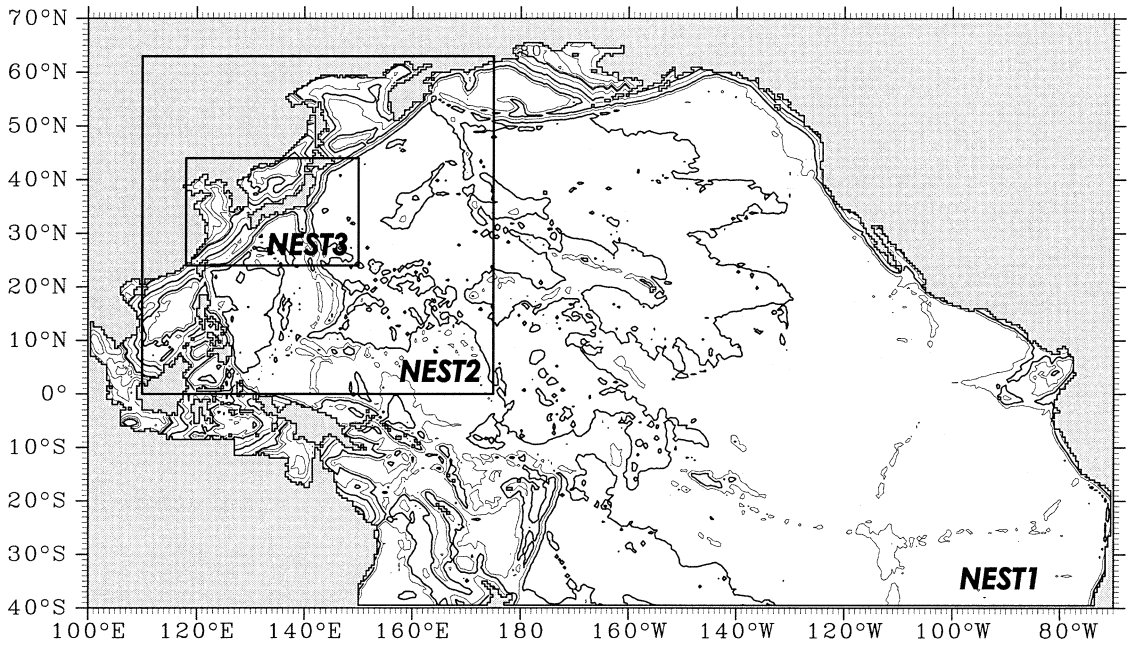

FIG. 2. Domain of triply nested models: NEST1, NEST2, and NEST3.

are compared with each other to demonstrate the importance of model resolution in simulating the Kuroshio and the related sea level variation. In section 4, we describe how the Kuroshio path in the ECS is affected by the model resolution, showing the important role played by JEBAR in determining the Kuroshio veering latitude west of Kyushu. Last, conclusions are given in section 5.

2. Numerical model

The Princeton Ocean Model (POM) is a three-dimensional primitive equation ocean model. It includes thermodynamics and the level-2.5 Mellor–Yamada turbulence closure and uses a sigma coordinate in the vertical to resolve the variation of bottom topography (Blumberg and Mellor 1987; Mellor 1998). Originally, the POM was designed for coastal waters since the sigma-coordinate system can well resolve complex topography in the coastal region. However, it has also successfully simulated large-scale ocean circulations in recent years. For example, the POM has been used to simulate the Kuroshio in the Pacific Ocean basin model (Kagimoto and Yamagata 1997) and the Gulf Stream in the Atlantic Ocean basin model (Ezer and Mellor 1997). For our purpose to investigate the open ocean–coastal sea interactions, both the open ocean and coastal sea, are of equal importance; to choose the POM as our basic model seems natural.

The grid ratio between a coarse model and a fine model is an important factor in constructing a nested model. Spall and Holland (1991) suggested that grid ratios of 3:1 and 5:1 should be used in nested model calculations, based on their estimate of the root-mean-square errors. Although their suggestion is based on a two-way nested model, it is likely to remain true in our case as well and is followed in this study. To achieve high resolution in the Kuroshio region, we use the 3:1 grid ratio twice to decrease the grid size from ½° (NEST1) to 1/18° (NEST3). We use the same sigma levels for all three models (see Table 1) since our main concern is the effect of changing the horizontal resolution.

The model topography of the Pacific Ocean is based

TABLE 1. Values of sigma coordinates used in the NEST1, NEST2, and NEST3.

Layer	Sigma coordinate
1	0.000
2	−0.002
3	−0.004
4	−0.010
5	−0.020
6	−0.040
7	−0.060
8	−0.080
9	−0.100
10	−0.120
11	−0.140
12	−0.170
13	−0.200
14	−0.300
15	−0.400
16	−0.500
17	−0.650
18	−0.800
19	−0.900
20	−0.950
21	−1.000

on Digital Terrain Model 5 [DTM5: Geophysical Exploration Technology (GETECH) 1995], which covers the global ocean with $5' \times 5'$ resolution. In coastal waters of Japan that cover three areas (34°–46°N, 135°–148°E; 30°–38°N, 128°–144°E; and 24°–30°N, 122°–132°E), the topography data with 500 m × 500 m resolution prepared by the Japan Oceanographic Data Center (JODC) are used. Two modifications are done to the original topography data: 1) setting the minimum (10 m) and maximum (6500 m) depths in the model and 2) smoothing the topography data to satisfy the following criteria (Mellor et al. 1994):

$$\frac{|H_{i+1} - H_i|}{(H_{i+1} + H_i)} \leq \alpha, \tag{1}$$

where, H_{i+1} and H_i are the depths at two adjacent grids and α is a slope factor set as 0.2.

Each model depth mapped in the NEST3 domain is shown in Fig. 3. The main differences between each panel of Fig. 3 are manifested in the shelf break region of the ECS and also around some seamounts. The smoothing changes the NEST1 topography rather drastically from realistic features. The NEST2 model topography is much improved but not enough, as seen in the difference of the spaces between the 200- and 1000-m isobaths in NEST2 and NEST3. The NEST3 topography is almost the same as that on charts of the ECS.

The models are driven by wind stresses, heat fluxes, and salt fluxes applied at the sea surface. The heat and salt fluxes are of a Haney type [see (26) in Barnier (1998)]. The coefficient used in the retroaction term is 35 W m^{-2} K^{-1} for the heat flux and 10 m $month^{-1}$ for the salt flux.

Figure 4 shows a designed schedule of model runs and the sources of each forcing data. The NEST1 and NEST2 models are both forced to run from rest state with the annual mean temperature and salinity of WOA94 (Levitus et al. 1994; Levitus and Boyer 1994), while the NEST3 model starts from the initial condition interpolated from the NEST2 results. During their spin-up phase, NEST1, NEST2, and NEST3 are integrated for 20, 15, and 3 years, respectively; they are forced by the monthly wind stresses (Hellerman and Rosenstein 1983), the monthly heat fluxes (da Silva et al. 1994), zero salinity fluxes, the monthly sea surface temperature (SST), and the monthly sea surface salinity of WOA94. During their hindcast phase from September 1991 to December 1998, the weekly wind stresses from the satellite data of *ERS-1* and *ERS-2* (CERSAT: see more information online at http://www.ifremer.fr/cersat), and the weekly SST data blended with the ship, buoy, and bias-corrected satellite data (Reynolds and Smith 1994) are used instead of the monthly wind stresses and the monthly SST data.

The lateral boundary condition of NEST1 is treated as a solid boundary for simplicity. This simplicity is acceptable because its southern boundary is located at 40°S, far from the Kuroshio region. As for NEST2 and NEST3, the boundary condition is treated in the following manner. First, the depths of the fine grids along the boundary are set equal to those of the corresponding coarse grids. Next, along the boundaries of NEST2 and NEST3, the unknown variables, that is, elevation, velocity, temperature and salinity, are obtained by spatial (bilinear) interpolation of the NEST1 and NEST2 model variables saved during their runs every 3h and every 1h, respectively. The turbulent kinetic energy and a macroscale length of turbulence at the open boundaries are both set to a small value (10^{-10}) as in the POM.

Since bilinear interpolation does not conserve volume flux through the interface between the fine and coarse grid model, the normal external velocity is modified so that the net flux through the interface is conserved (see the appendix). These spatially interpolated variables are then used to specify the boundary conditions for each nested model in which temporal (linear) interpolation of the saved variables is made to fit data to the fine grid model at each time step. Table 2 summarizes the model domain and physical parameters of all three models.

3. Results

a. Mean sea level and velocity distributions

The mean sea level calculated by each model for the NEST3 domain and averaged over the years 1994–98 is shown in Fig. 5; data for the first two years, 1992–93, are not used because of the influence of switching from monthly to weekly forcing.

One of the most obvious differences among three models is the Kuroshio path in the ECS. The gradient of sea level across the Kuroshio, which measures the intensity of the Kuroshio surface current, becomes larger as the model resolution becomes finer. The Kuroshio main path, as remarked in the introduction, is estimated by tracing the steepest gradients of sea level in Fig. 5, for example, the contour lines of 30 cm in NEST1 and those of 20 cm in NEST2 and NEST3. The Kuroshio in NEST1 flows farther north than observed (Fig. 1) and its retroflection latitude is about 32°N. This overshooting of the veering latitude is improved a little by NEST2. Only the NEST3 model reproduces the correct eastward veering of the Kuroshio at 30°N. Other obvious differences in models are seen in the Japan Sea and east of Honshu; the Tsushima Warm Current and the Kuroshio Extension become more realistic as resolution increases.

The model mean currents at depth 20 m for the same domain and period are shown in Fig. 6. The region where velocity amplitudes exceed 50 cm s^{-1} is hatched rather than arrowed. This figure illustrates the importance of horizontal resolution to simulate the strong ocean currents such as the Kuroshio and the Tsushima Warm Current. Comparison with the observed current data (Fig. 1) shows that the Kuroshio reproduced by NEST1 is much weaker and wider in the ECS. To the

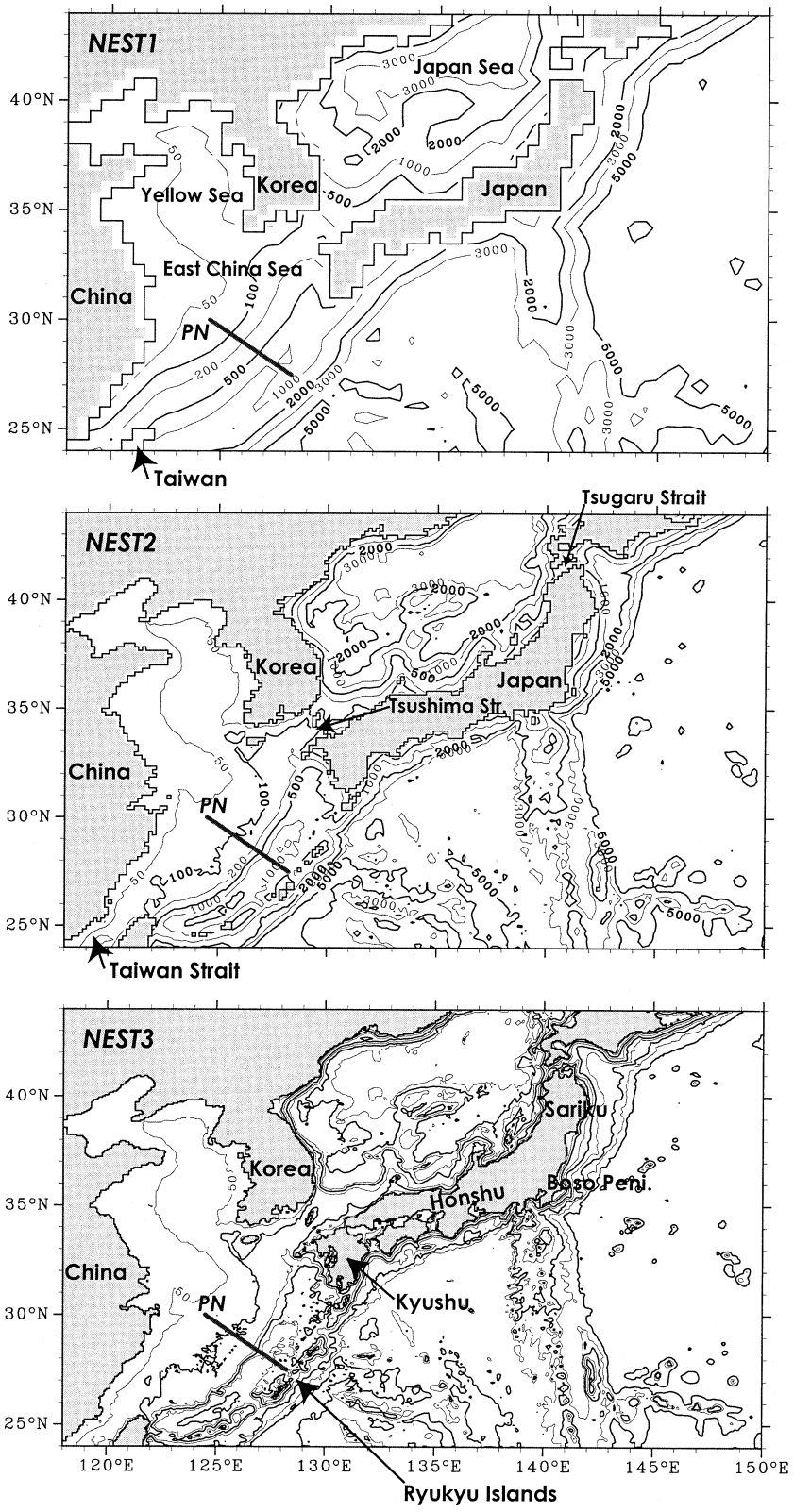

FIG. 3. Model depths (m) mapped for the NEST3 domain: PN denotes the observational hydrographic line in the East China Sea (known as the PN line).

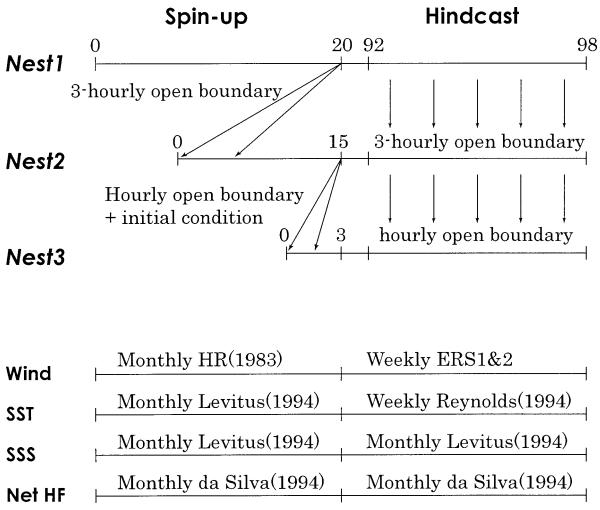

FIG. 4. Schedule for model run and data sources. Schematic of model runs (top rows); units of spinup and hindcast phases are in years and calendar years, respectively; slanted and vertical arrows show how initial and boundary conditions of nested models are obtained (see text for explanations). Data sources used to drive models (bottom rows) are HR: Hellerman and Rosenstein wind stress data, SST: sea surface temperature data, SSS: sea surface salinity data, and Net HF: heat flux data.

south of Japan, it is also weaker than the realistic one and cannot form a jetlike current, particularly in the Kuroshio Extension region. The Kuroshio reproduced by NEST2 is much stronger than that of NEST1, but the retroflection (veering) latitude in the ECS is too far northward. Also, after leaving the eastern coast of Honshu, the Kuroshio overshoots to the north. However, with increasing resolution, the NEST3 model with a resolution of $\frac{1}{18}^\circ$ resolves the Kuroshio in a realistic way, both in strength (larger than 1 m s^{-1}) and path.

There are many other improved features in NEST3. These are 1) the shelf circulation in the ECS, 2) the currents in the Yellow Sea, 3) the Tsushima warm current flowing into the Japan Sea, 4) the southward current along the west coast of Kyushu, 5) the Kuroshio countercurrent west of the Ryukyu Islands, 6) the warm recirculation eddy south of Japan, and 7) the Tsugaru warm current along the Sanriku coast.

b. Variability of sea surface height

Here we calculate the square root of the standard deviation in order to see how the sea surface height variability changes with increasing the model resolution. It is defined as

$$\sqrt{\frac{1}{N-1}\sum_{i=1}^{N}(\eta_i - \overline{\eta})^2},$$

where η_i and $\overline{\eta}$ denote the sea surface height of the ith data in a time series and the average of η_i over all data N of that time series, respectively (e.g., Emery and Thomson 1998). We simply refer to this quantity as rms (root mean square). Figure 7 shows this distribution reproduced by each model for the NEST3 domain and during the years 1994–98. Also shown on the bottom right, marked T/P, is the rms distribution calculated from the satellite TOPEX/Poseidon data [World Ocean Circulation Experiment (WOCE) global data from the Jet Propulsion Laboratory (JPL)].

It is clearly seen that the rms changes remarkably with the model resolution. In the NEST1 results, we find three separate regions with rms values over 8 cm, each located around the Ryukyu Islands, south of Japan, and east of Honshu. With increasing resolution, these regions are merged into one large area with enhanced rms amplitudes. Such change is related to the more realistic resolution of mesoscale eddies in the finer grid models.

One noticeable area that is strongly sensitive to the model resolution is the Kuroshio Extension region. The satellite altimeter gives a maximum rms of about 40 cm there. The rms variability in this area produced by NEST1 and NEST2 shows a maximum of about 10 and 24 cm, respectively; these values are much smaller than those observed. The variability reproduced by NEST3 shows a maximum of about 32 cm, a value much closer to the observed value. However, its distribution east of Honshu differs a little from that of TOPEX/Poseidon. The influence of the eastern boundary, where the NEST2 results are fixed, may be inevitable in this region. One obvious point is that the overshooting of the Kuroshio Extension in NEST2 leads partly to a more northward position of the Kuroshio Extension in NEST3, which might alter the rms distribution of sea level in NEST3

TABLE 2. Domain and parameters used in the triply nested model. The meanings of SLMIN, HORCON, TPRNI, DTE, and DTI can be found in the users guide of POM (Mellor 1998).

Model	Domain	Grid size (deg)	SLMIN	HORCON	TPRNI	DTE (s)	DTI (min)
NEST1	40°S–70°N 100°E–70°W	1/2	0.2	0.1	0.5	36	18
NEST2	0–63°N 110°–175°E	1/6	0.2	0.1	0.5	12	12
NEST3	24°–44°N 118°–150°E	1/18	0.2	0.1	0.5	6	6

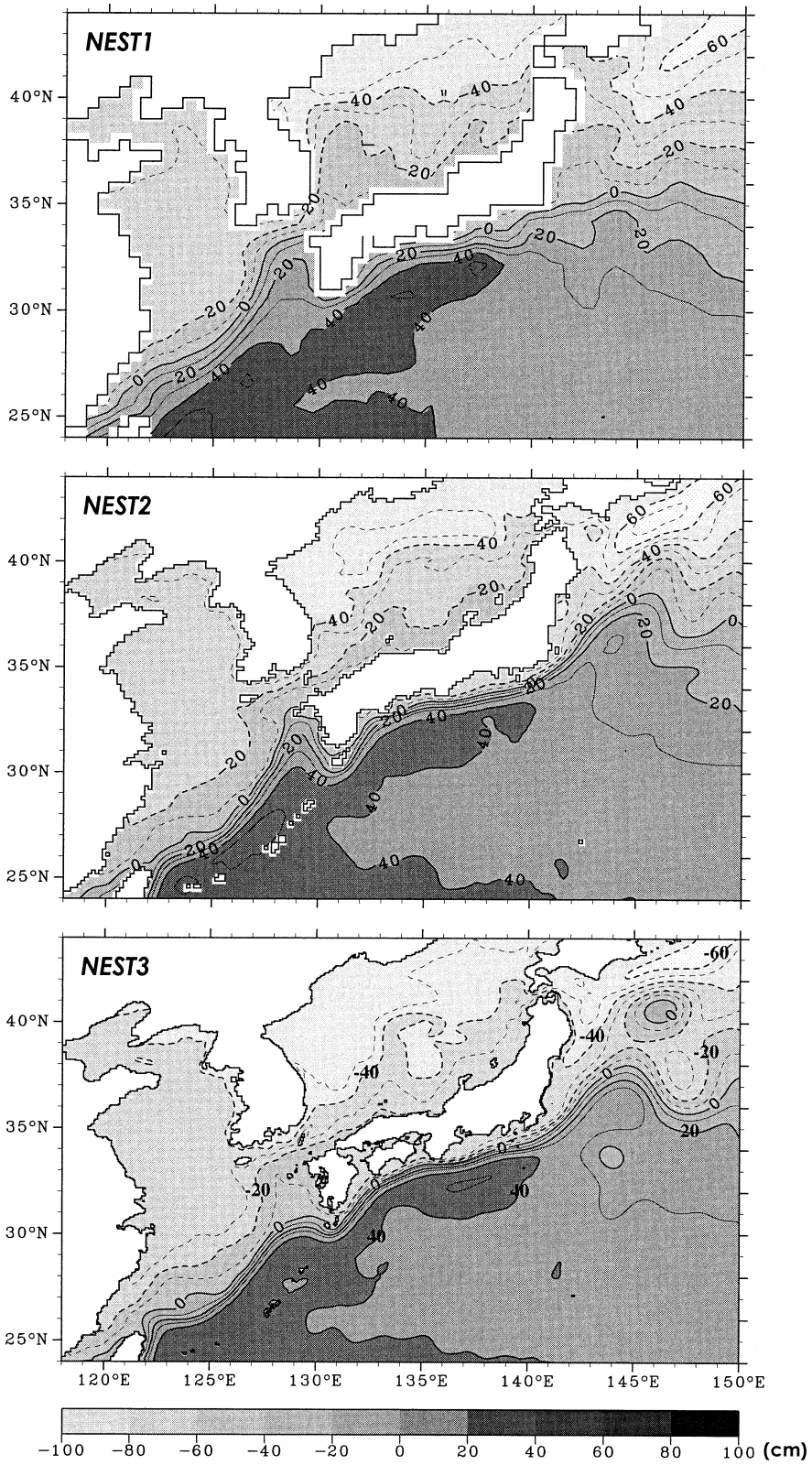

FIG. 5. Mean sea levels of three models for the NEST3 region; values on contour lines represent those of hindcast results averaged over the years 1994–98.

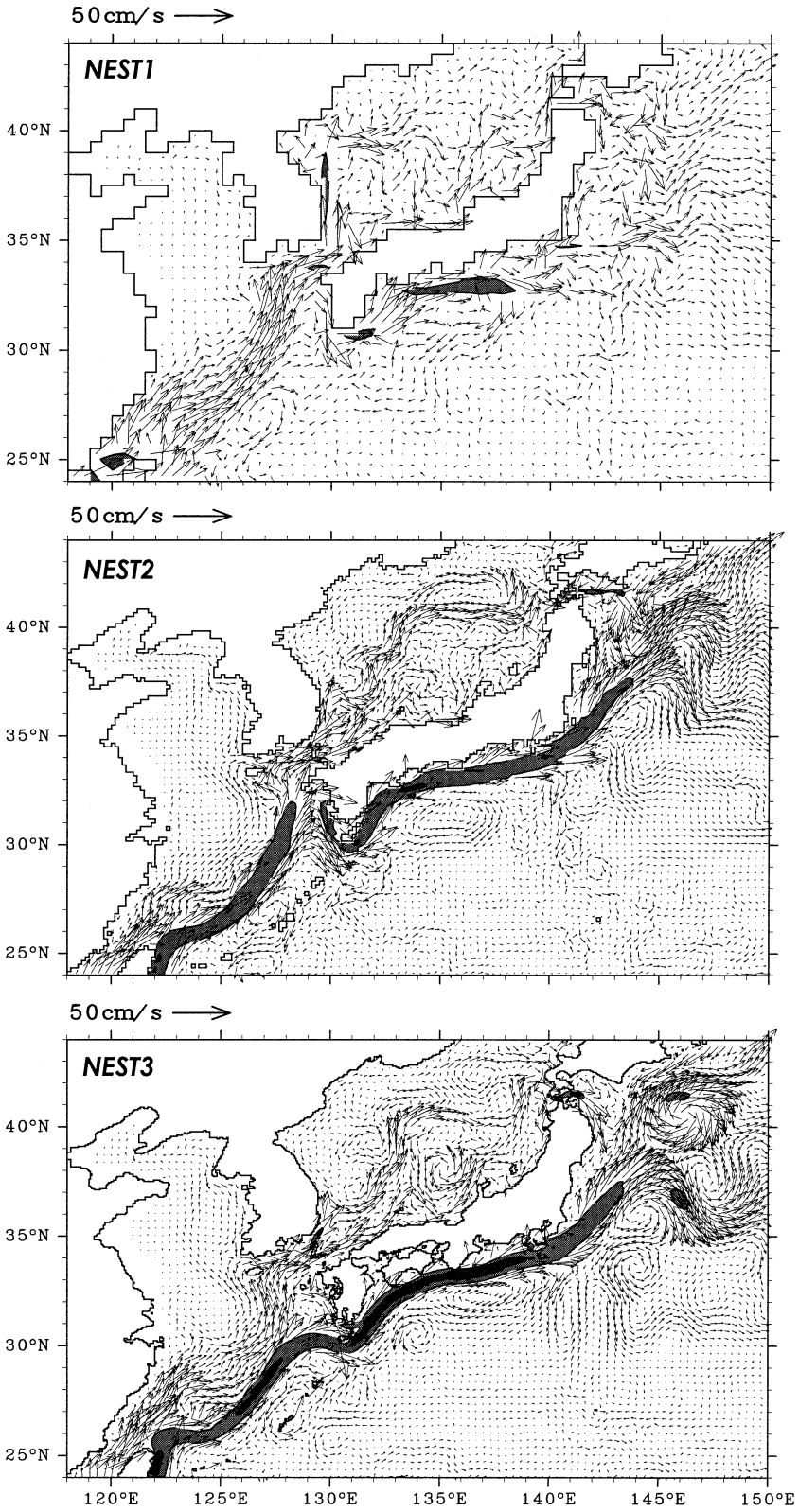

FIG. 6. As in Fig. 5 but for the mean velocity at depth 20 m; regions where current speeds are over 50 and 100 cm s^{-1} are hatched with shallow and deep tones, respectively, rather than arrowed; arrows for NEST2 and NEST3 are drawn every two and six grid points, respectively.

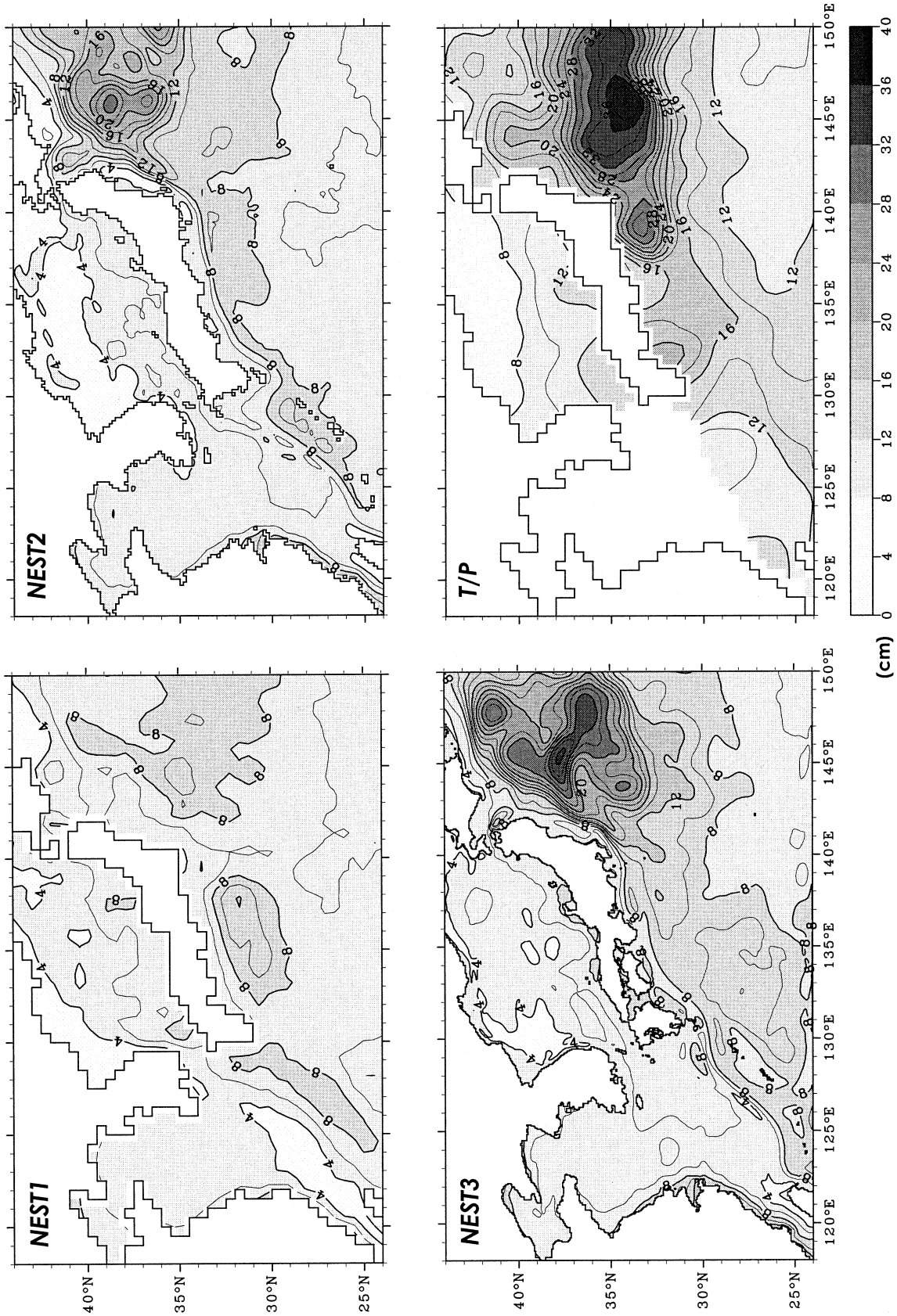

FIG. 7. As in Fig. 5 but for rms of sea surface height (see text for definition); T/P in the bottom-right picture represents rms calculated from TOPEX/Poseidon data (contour interval is 2 cm). Because of tidal correction problem, data in the Yellow Sea and a part of ECS are not included in T/P dataset.

to be different from that of TOPEX/Poseidon data. This is a weak point of the one-way nested model. To solve this, we must use a two-way nested method. An alternative is to shift the eastern boundary of the NEST3 model farther east of the Kuroshio Extension region.

c. Vertical structure and volume transport across PN line

As a typical transect in the ECS, the PN line (see Fig. 3 for its position) provides a good location to compare our model results with the observed data; it also enables us to demonstrate how model results are sensitive to changes in grid size.

In Fig. 8 we show the vertical section of the alongshelf velocity component, potential temperature, and salinity distributions on the PN line reproduced by each model. In general, all three models simulate a strong current core, that is, the Kuroshio, in the surface layer just above the shelf break. Since the shape of the shelf/slope is improved with model resolution, the geographical location of the Kuroshio core is also improved with resolution. We see that the area and intensity of the core and the vertical shear of the alongshelf current are all very sensitive to model resolution. For example, the surface speed changes from 40 cm s^{-1} in NEST1 to 110 cm s^{-1} in NEST3. This is associated with the change of the vertical shear of the Kuroshio. In contrast to these local features, the total volume transport through the PN line changes little as shown in the left three panels of Fig. 8. The total transport must be determined by the larger scale dynamics (Kagimoto and Yamagata 1997).

The water temperature and salinity distributions change gradually as the model resolution increases. With increasing Kuroshio core speed, however, the isotherms and isohalines around the core become slanted. This means that the horizontal gradient for both water temperature and salinity increases. The distribution of the density field is similar to that of the temperature field in this area (e.g., see Fig. 17).

The above features of the alongshelf velocity, water temperature, and salinity along the PN line are explained in terms of the *thermal wind relation,* which relates the horizontal density gradient with the vertical shear of the alongshelf velocity component. As already remarked, there is not much change in the volume transport among the three models because the driving forces (wind stresses and heat fluxes) are the same in all three models. Thus, in order to conserve the volume transport, the surface (bottom) current must become larger (smaller) as the vertical shear of the current increases.

Using hydrographic data for the years 1988–94 and assuming a level of no motion at depth 700 m, Oka and Kawabe (1998) calculated the geostrophic current across the PN line for four seasons. Compared with the annual mean distribution of geostrophic currents, potential temperature, and salinity fields at this section (Fig. 9), the results of NEST3 are consistent with these observed data. In particular, the vertical shear of current is well reproduced by NEST3.

When compared with the NEST3 result, the velocity distributions in NEST1 and NEST2 are more barotropic in the vertical profile. Kagimoto and Yamagata's (1997) result of a ⅓° model also shows the weaker vertical shear of currents compared to the NEST3 result. Increasing the horizontal resolution also leads to a water temperature distribution close to the observed one associated with the large horizontal gradient across the Kuroshio. Thus we conclude that the model Kuroshio becomes more baroclinic as the model horizontal resolution increases.

The volume transport across the PN line is often used to represent the Kuroshio transport typical in the ECS. Based on the hydrographic data observed along the PN line from 1973 to 1993, Hinata (1996) suggested, assuming a reference depth of no motion at a depth of 700 m, that the mean geostrophic volume transport through the PN line is 25.4 Sv (Sv $\equiv 10^6$ m^3 s^{-1}) with a little decrease in autumn. By assuming no motion at 700 m artificially in our model and integrating vertically the alongshelf velocity across the PN line, we can compare the model transport with Hinata (1996)'s result. Besides this estimate, we give another estimate of the volume transport integrated from 700 m to the surface, in which the velocity at depth 700 m is not zero. The difference between these two transports is the barotropic component of the Kuroshio transport defined at depth 700 m. In Table 3, we show these two volume transports calculated from the results as shown in Fig. 8.

Though the values in Table 3 are a little smaller than that given by Hinata (1996), the volume transport from 700 m to the surface does increase as the model resolution is increased. The interesting feature in Table 3 is the trend among the three models toward decreasing the barotropic component of the Kuroshio transport with increasing resolution (i.e., 7.6, 3.5, and 2.2 Sv in the order of NEST1, 2, and 3). This trend is consistent with the reduction of the bottom velocity on the slope with increasing the resolution. This aspect is important in modeling the Kuroshio path correctly since the presence of bottom velocity on the slope enables the interaction between the bottom topography and ocean current, keeping the Kuroshio path along isobaths (Warren 1963).

4. The Kuroshio veering at 30°N in the ECS

a. Effects of model resolution on JEBAR

As is observed, the Kuroshio flowing to the northeast along the shelf break of the ECS suddenly turns to the east at 30°N west of Kyushu. The existence of Kyushu and Tokara Strait is the primary cause for this turn because the ocean current is expected to flow, at first approximation, along the f/H contours (f and H being the Coriolis parameter and the water depth, respectively)

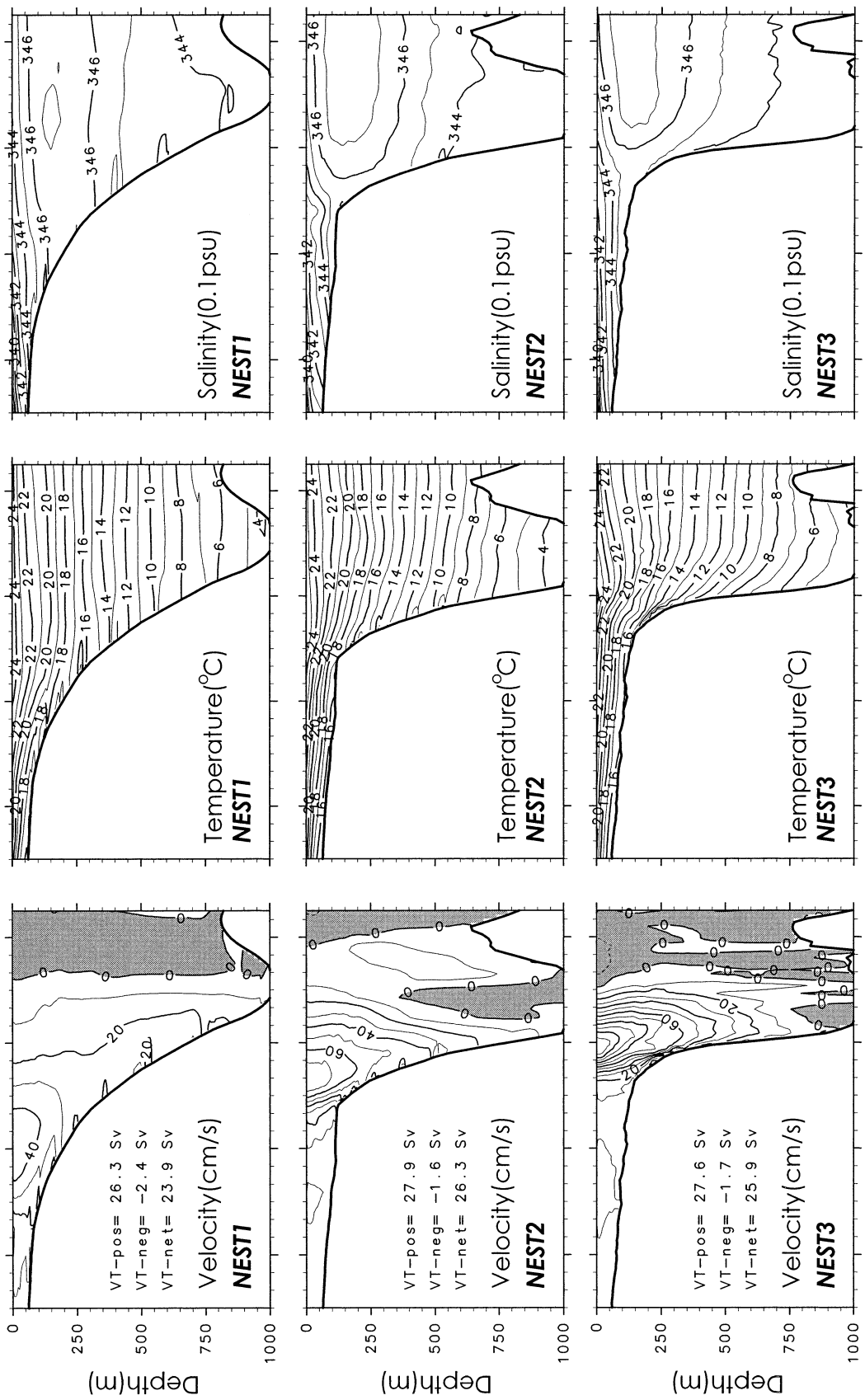

FIG. 8. Vertical distribution of model results at PN line: (left) alongshelf velocity, (middle) potential temperature, and (right) salinity. Regions with negative values of alongshelf velocity are shaded; model-calculated volume transports are shown in left panels (VT-pos and VT-neg are volume transports calculated with positive and negative alongshelf velocity, respectively; VT-net represents a sum of VT-pos and VT-neg).

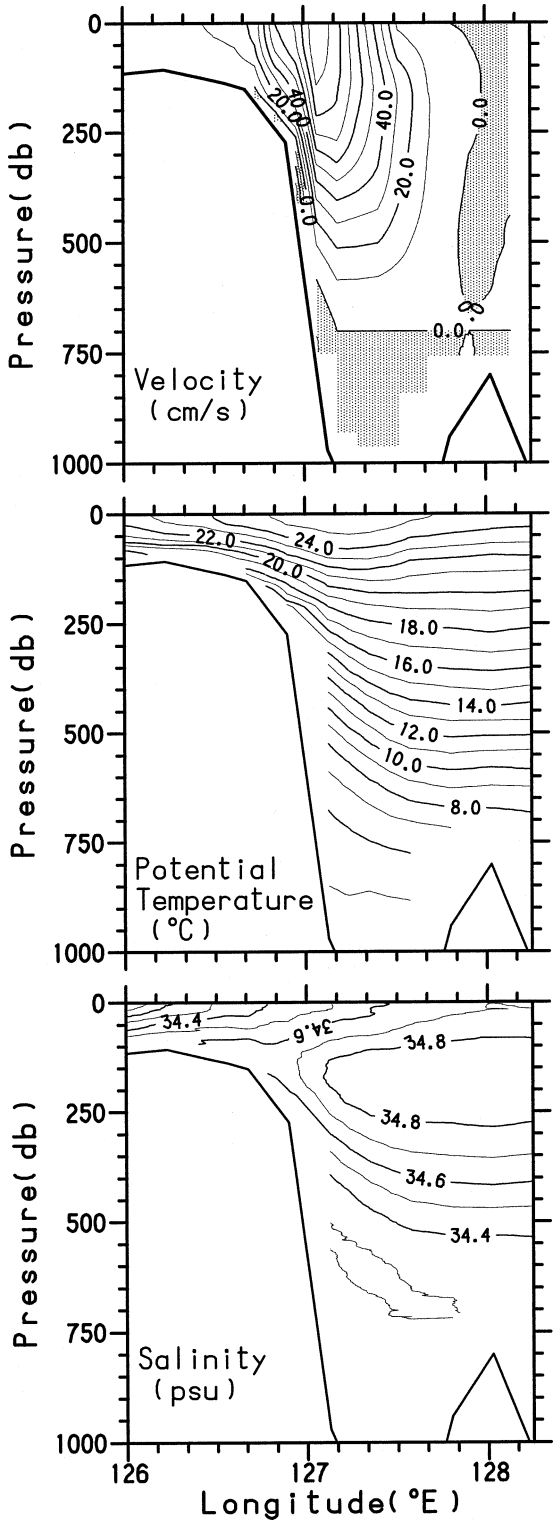

FIG. 9. Vertical distributions of observed data at PN line for (top) alongshelf geostrophic velocity with reference depth of no motion at 700 dbar, (middle) potential temperature, and (bottom) salinity. Regions with negative values of alongshelf velocity are shaded.

when the relative vorticity is much smaller than the planetary vorticity. However, notice that the contours at 200 and 500 m in Fig. 3, which correspond to the shelf break in the ECS, extend up to 32°N west of Kyushu, 2°N farther north of the veering latitude. Therefore, the Kuroshio does not exactly follow the f/H contours, so there should be some other mechanisms deflecting the Kuroshio from the f/H contours.

To see this more clearly, we show in Fig. 10 the vertically integrated current field (from surface to a depth of 1000 m) for the three models, along with the f/H contours. The Kuroshio in the NEST3 model flows along the f/H contours in the ECS until it reaches west of Yakushima located near 30°N, 130°E. Then the Kuroshio crosses the f/H contours to enter Tokara Strait. Apart from this feature, the NEST3 model also shows the presence of the Ryukyu Current, the current flowing northeastward along the eastern offshore of the Ryukyu Islands (Yuan et al. 1995). This is the advantage of using a high-resolution model that can resolve the small-scale seamounts such as the Ryukyu Islands.

Concerning the Kuroshio veering, three models produced the following features: three eastward branch currents located at 28°, 30°, and 32°N in NEST1; a wide eastward current ranged from 30° to 32°N in NEST2; and a coherent jetlike current that turns, as in the observation, to the east at 30°N in NEST3. From these results, we see that the deflection of the Kuroshio from the f/H contours becomes more prominent as model resolution is improved.

To analyze the Kuroshio veering, we consider the offshore/onshore volume transport across the shelf break. If we decompose the Kuroshio currents into the velocities parallel and perpendicular to the f/H contours, the Kuroshio veering may be regarded as a phenomenon in which the offshore transport exists and is maintained by some mechanism.

To make this idea concrete, we start from the primitive equations. After vertically averaging the momentum equations and then taking a curl, we obtain the following vorticity equation:

$$\frac{\partial}{\partial t}\,\mathrm{curl}_z\left(\frac{\mathbf{M}}{H}\right) + \mathbf{M}\cdot\nabla\left(\frac{f}{H}\right) = J(\chi, H^{-1}) + \mathrm{curl}_z\left(\frac{\boldsymbol{\tau}_a}{\rho_0 H}\right) - \mathrm{curl}_z\left(\frac{\boldsymbol{\tau}_b}{\rho_0 H}\right) + \mathrm{curl}_z\left(\frac{\mathbf{D}}{H}\right) - \mathrm{curl}_z\left(\frac{\mathbf{A}}{H}\right). \quad (2)$$

In (2), two operators are defined as

$$J(A, B) = \frac{\partial A}{\partial x}\frac{\partial B}{\partial y} - \frac{\partial A}{\partial y}\frac{\partial B}{\partial x} \quad \text{and}$$

$$\mathrm{curl}_z(\mathbf{A}) = \frac{\partial A_y}{\partial x} - \frac{\partial A_x}{\partial y};$$

TABLE 3. Volume transport through the PN line calculated from the results of three models shown in Fig. 8: VT_{total} is defined as $\int (\int_{700m}^{0} V\,dz)\,dl$, and VT_{ref} is $\int (\int_{700m}^{0} (V - V_{700m})\,dz)\,dl$, where dl expresses the integrating along the PN line.

Model	VT_{total}	VT_{ref}	$VT_{total} - VT_{ref}$
NEST1	22.2	14.6	7.6
NEST2	25.6	22.1	3.5
NEST3	25.7	22.8	2.9

also, $\mathbf{M} = \int_{-H}^{0} (u\mathbf{i} + v\mathbf{j})\,dz$ is a volume transport vector, $J(\chi, H^{-1})$ the JEBAR term with $\chi = \int_{-H}^{0} zg\rho/\rho_0\,dz$ being the potential energy, $\boldsymbol{\tau}_a$ the wind stress, and $\boldsymbol{\tau}_b$ the bottom stress. Two other vectors $\mathbf{D} = D_x\mathbf{i} + D_y\mathbf{j}$ and $\mathbf{A} = A_x\mathbf{i} + A_y\mathbf{j}$ are the vertically integrated horizontal diffusion term and the nonlinear advection term, respectively.

When one considers a mean state of the Kuroshio such as shown in Fig. 10, the first term in (2) is neglected. The second term on the left-hand side of (2) represents the advection of the geostrophic potential vorticity f/H (hereinafter referred to as APV). This term is also interpreted as giving a transport across the f/H contours and should be balanced by the right-hand side (rhs) terms of (2) in a steady state. Then, three cases are possible depending on the sign of rhs. If APV $= 0$, the transport is exactly along the f/H contours. If APV > 0, the transport is in the onshore direction and the Kuroshio tends toward the continental shelf of the ECS. But if APV < 0, the transport is in the offshore direction and the Kuroshio tends toward the deep ocean. Thus, the Kuroshio veering must be associated with the case of APV < 0.

Using the model data averaged over the years 1994–98, we calculated all terms in (2) except for the time variation term and mapped their values. Figure 11 is for APV. Comparing Fig. 11 with Fig. 10, we find that a large positive value exists from the northeast of Taiwan through the west of Kyushu in the NEST1 model. This agrees well with the transport distribution of the NEST1 model in Fig. 10, which shows the general tendency of currents ascending the shelf region. As the model resolution is increased, the map of APV changes drastically. The large elongated area with a positive value along the shelf break splits into many small patchlike areas with alternate signs. The Kuroshio veering area west of Kyushu corresponds to the area with a large negative value around 32°N in NEST2 and that around 30°N in NEST3.

The next problem is to identify contribution to this offshore transport across the f/H contour. As we will see, it is mainly due to the JEBAR term. Figure 12 shows maps of JEBAR, the first term on the rhs of (2), for the three models. The JEBAR shows a pattern similar to that of APV for all three models, particularly along the shelf break of the ECS and at the southern coast of Japan. This suggests that the offshore advection of f/H is mainly balanced by JEBAR, regardless of the model resolution. Away from the shelf break, however, the distribution pattern is different between Fig. 11 and Fig. 12. For example, the distribution of APV over the shallow sea area northeast of Taiwan Strait and over the Chinese coastal sea area cannot be explained only by the JEBAR forcing.

Three curl terms of wind and bottom stresses and nonlinear advection in (2) are shown in Fig. 13 for the NEST3 model. Interestingly, the curl of the nonlinear advection term shows a very fine structure similar to those in Figs. 11 and 12, while the wind and bottom stress curls show more definite patterns. The curls of nonlinear advection and bottom stress both give a dominant balance against the APV term only over the shallow sea area northeast of Taiwan Strait extended to the ECS continental shelf, where the JEBAR term is small.

Along the Chinese east coast and the shelf break, the curl of wind and bottom stresses dominates and shows a definite sign; such features are simply interpreted in terms of the Ekman flux divergence (convergence) and the associated vortex stretching (shrinking) in the whole water column, which in turn pushes the fluid with f/H towards onshore (offshore; e.g., Hukuda et al. 2001). The remainder is very difficult to interpret in a simple way because of its fractal-like feature as seen in each map of APV, JEBAR, and the nonlinear advection term for NEST3. These features are caused by higher order spatial derivative terms augmented with increasing the resolution of bottom topography and flow nonlinearity.

As clearly seen in Fig. 12, we note that the amplitude and sign of the JEBAR term depend strongly on the model resolution. As discussed before, both horizontal density gradient and bottom topography approach the realistic observed feature as the model resolution is increased. Thus, a high-resolution model is necessary to correctly reproduce the JEBAR term, which in turn influences the path of the Kuroshio in the ECS.

To quantify the above discussion on the Kuroshio veering at 30°N, we checked the values of all terms in (2) over the block enclosed by 28°–30°N, 126°–128°E as indicated in Figs. 10–13. This area is located just upstream of the Kuroshio veering location, and thus the vorticity balance in this area is directly responsible for the Kuroshio veering. Table 4 shows the values of all terms in (2) integrated over the area. As expected, both NEST1 and NEST2 models give positive values of APV, thus implying the Kuroshio's onshore transport of f/H. The NEST3 model, however, gives a negative value of APV, thus implying the Kuroshio's offshore transport of f/H. This result is consistent with Fig. 10. From Table 4, the JEBAR term gives a dominant contribution to APV and explains well the path change of the Kuroshio as the model resolution increases from low (NEST1, NEST2) to high (NEST3).

The analysis in this subsection demonstrates that a large offshore transport of f/H accompanied with the Kuroshio veering is related to the JEBAR. The change of veering position in the three models may also be

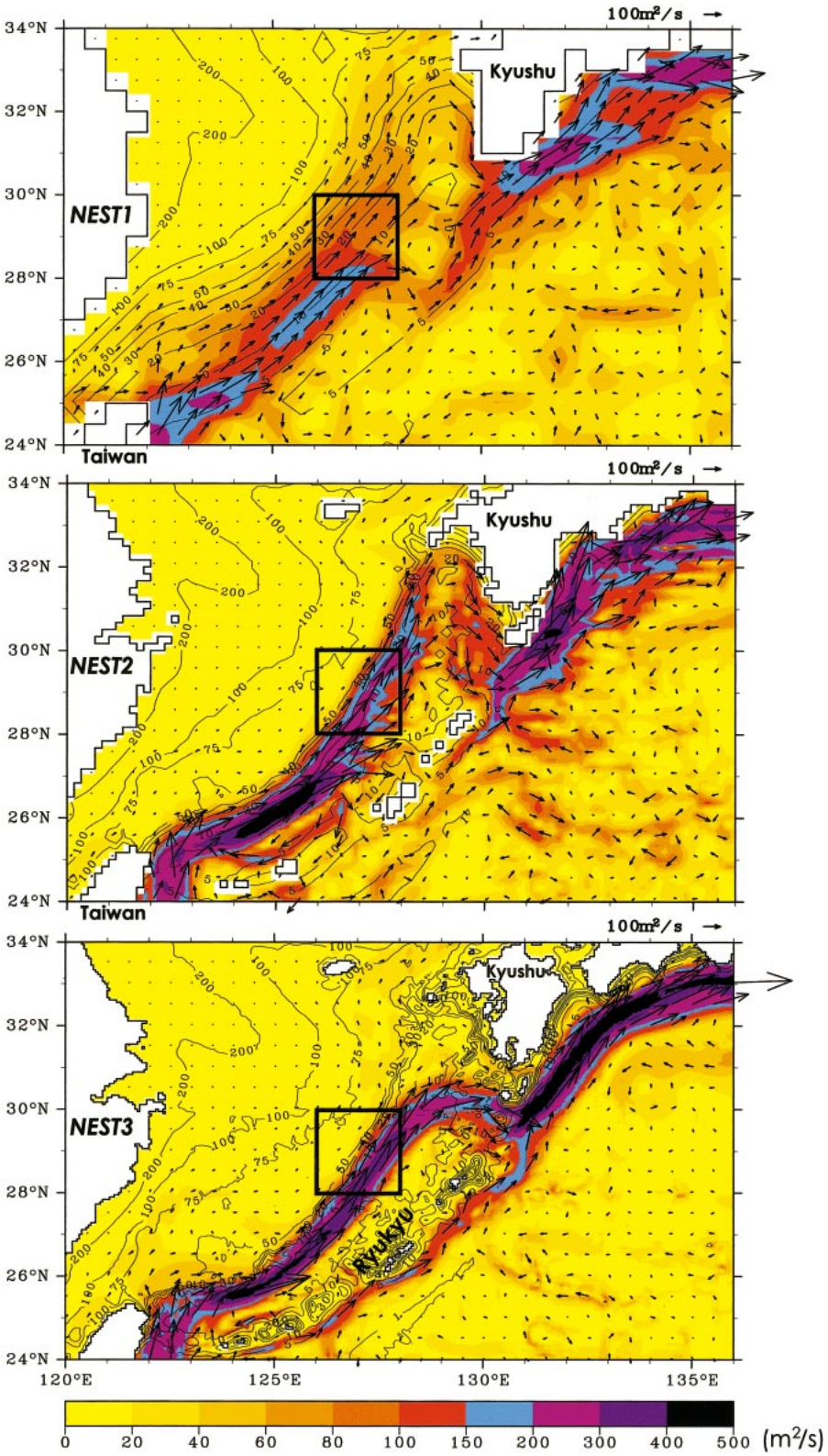

FIG. 10. Model transport (integrated from the surface down to 1000 m) shown with both vector and shading for a part of NEST3 domain (f/H contour values are also shown in units of 10^{-8} m^{-1} s^{-1}). Boxes are used for calculations of Figs. 15 and 16 and Table 4.

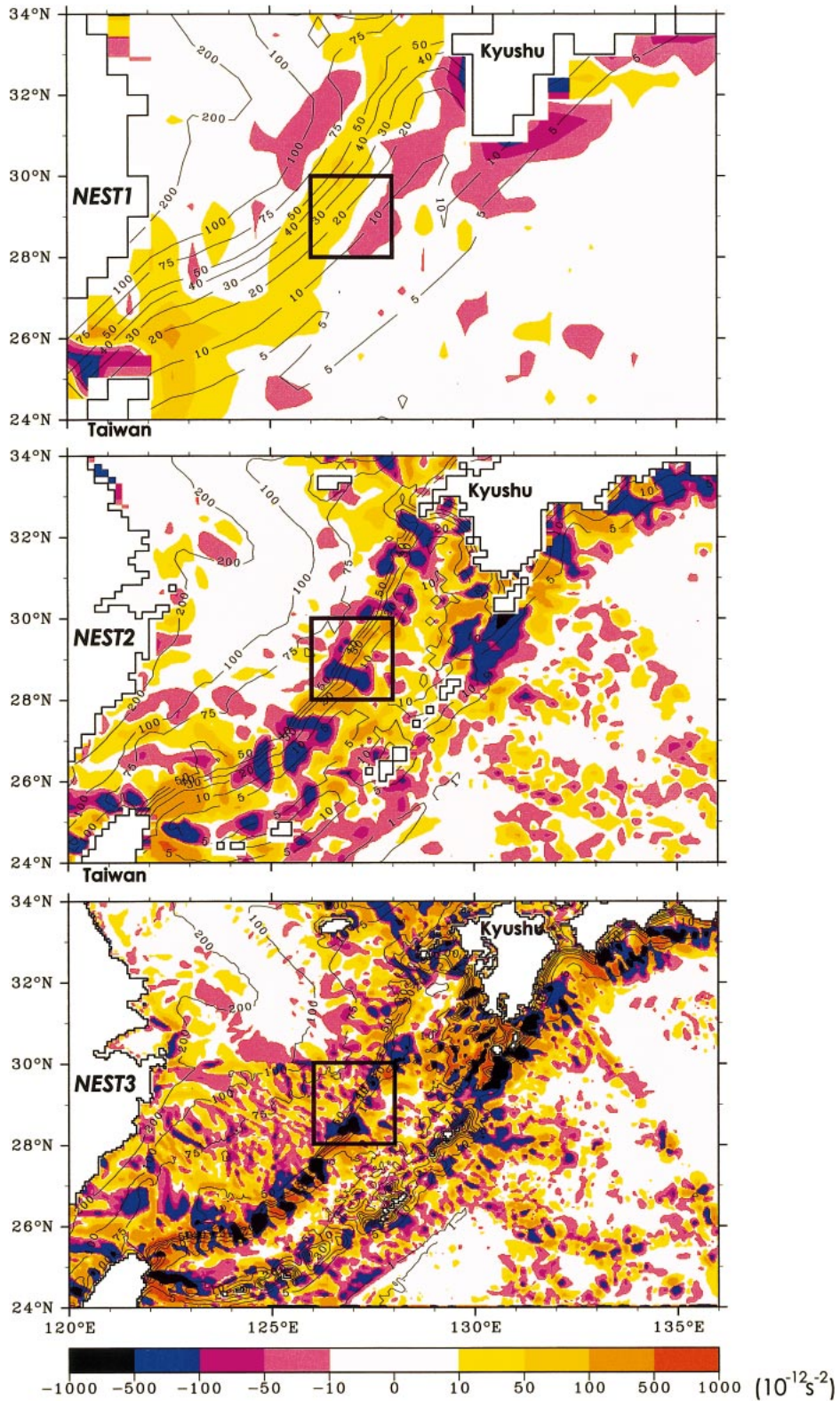

FIG. 11. Maps of APV term for the same area as in Fig. 10; values are calculated from mean model fields averaged over the years 1994–98.

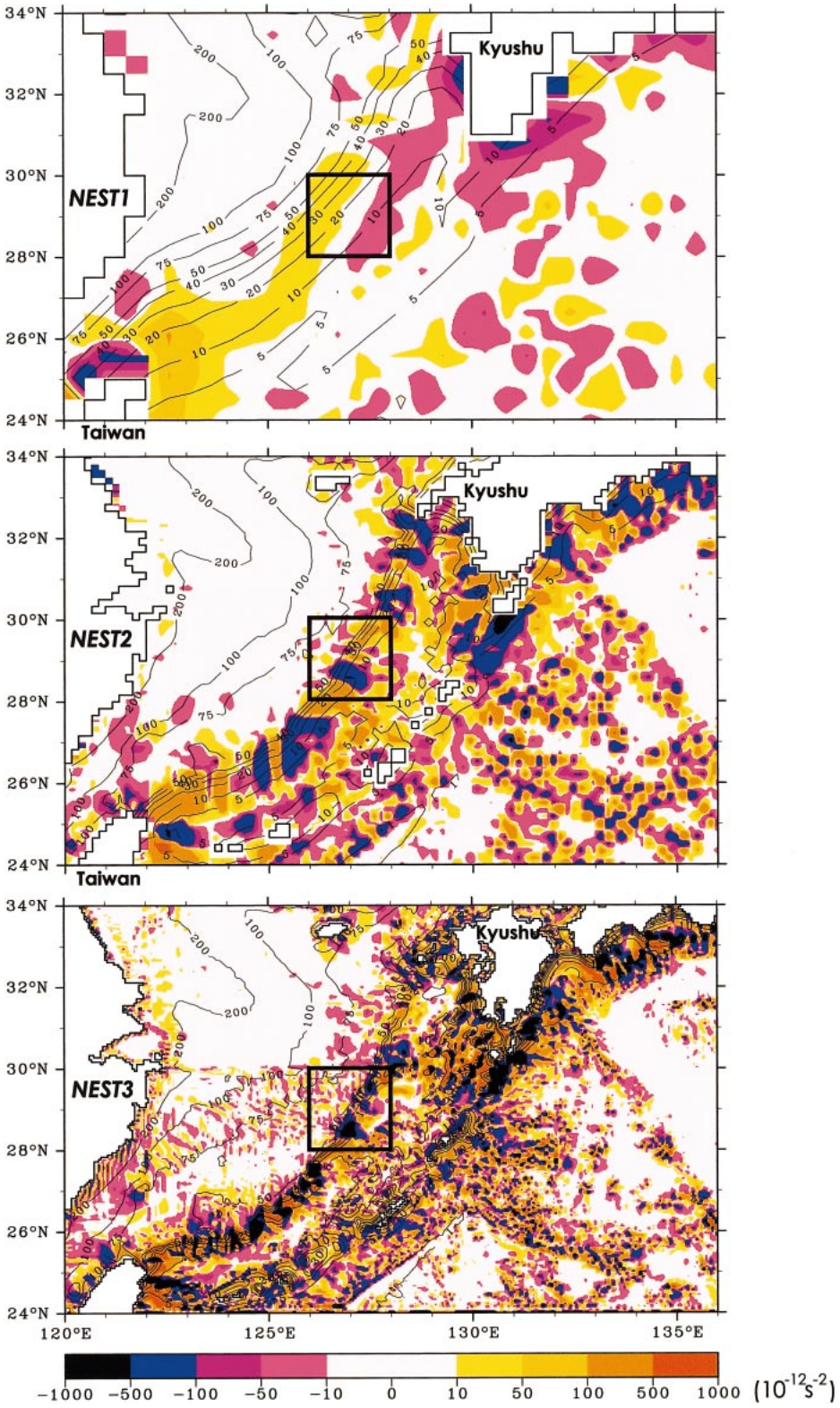

FIG. 12. As in Fig. 11 but for JEBAR; note similarity between Figs. 12 and 11.

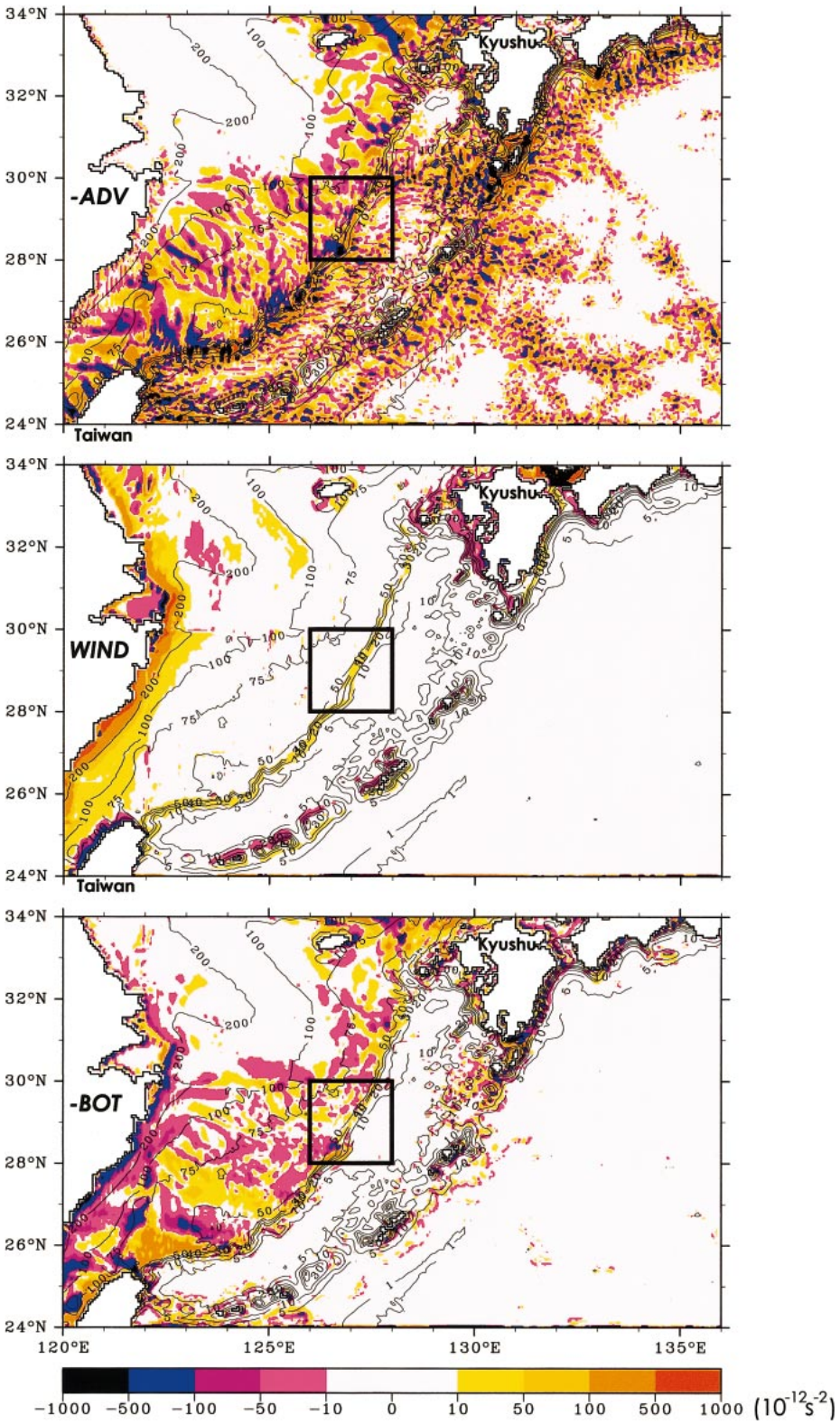

FIG. 13. Maps of the three terms related to nonlinear advection, wind stress, and bottom stress in (2) calculated from NEST3 results.

TABLE 4. Area-integrated values ($m^2\ s^{-2}$) of all the terms in (2) except for the time variation term over the block shown in Fig. 10. The total area is $4.3358 \times 10^{10}\ m^2$.

Model	$\mathbf{M}\cdot\nabla\left(\frac{f}{H}\right)$	$J(\chi, H^{-1})$	$\mathrm{curl}_z\left(\frac{\boldsymbol{\tau}_a}{\rho_0 H}\right)$	$-\mathrm{curl}_z\left(\frac{\boldsymbol{\tau}_b}{\rho_0 H}\right)$	$\mathrm{curl}_z\left(\frac{\mathbf{D}}{H}\right)$	$-\mathrm{curl}_z\left(\frac{\mathbf{A}}{H}\right)$
NEST1	0.440	0.123	0.086	0.116	0.005	0.092
NEST2	0.636	0.655	0.167	0.103	−0.003	−0.303
NEST3	−0.553	−0.820	0.167	0.179	−0.003	−0.056

understood from another viewpoint of the current above the shelf slope. Figure 14 presents the current distribution in the bottom layer (sigma = −0.975) over the shelf slope of the ECS. Obviously, with increasing model resolution, the velocity in the bottom layer decreases (see also Fig. 8). As shown in the previous section, the effect of model resolution is to increase the baroclinicity and to decrease the barotropic transport of the Kuroshio. The low-resolution model is thus more barotropic than the high-resolution model and more susceptible to topographic control with a strong current at the bottom. This explains why the Kuroshio in the NEST1 and NEST2 models tends to follow the topography and extend too far northward, whereas the Kuroshio in the NEST3 model turns to the east as observed.

It is of interest to examine how each term in (2) varies with time and contributes to the shift of the veering position during the spinup of NEST3. Recall the schedule for model to spin up as shown in Fig. 4 and that the initial values of the NEST3 model are interpolated from the NEST2 model results. Then, as spinup progresses, the Kuroshio's retroflection latitude gradually shifts southward. After 120 days the Kuroshio path approached the mean position as shown in the bottom panel of Fig. 6. Figure 15 shows the temporal change of each term in (2) integrated over the same area as in Fig. 10 during the first year of spinup of NEST3. Both APV and JEBAR terms changed their signs by day 120. As shown in Table 4, we note that these two terms change signs as the model resolution is increased from NEST2 to NEST3. Figure 15 shows that this change occurred right after NEST3 has started spinning up. After having reached the negative maximum, the negative values stay almost the same, and there is no large major change in the basic vorticity balance afterward during the spinup stage.

The change of JEBAR must be associated with the variation of density in the area; the change of APV must be associated with the variation of currents. Figure 15 thus implies that the density and current fields vary simultaneously. This is consistent with the result in section 3, namely, that the Kuroshio in the ECS is approximately in geostrophic balance. Figure 15 cannot provide a causal relationship of the Kuroshio veering, but it provides a useful diagnosis that the JEBAR plays a predominant role over the remainder of rhs in (2).

All other terms are less essential to the Kuroshio veering since these terms show no drastic temporal change in Fig. 15. But a few points should be noted. The bottom stress curl has a positive value throughout the year and thus leads to an onshore transport at the shelf break, which contributes to producing positive vorticity in the interior geostrophic region (see Hukuda et al. 2001). The contribution from the wind stress curl has a modest seasonal variation. It also generates an onshore transport at the shelf break, as shown in Fig. 13. In summer, this direct wind contribution is small, but northerly winds in winter increase its magnitude, thus counteracting the JEBAR effect to some extent.

b. Seasonal migration of the Kuroshio veering position

Figure 15 suggests the existence of seasonal variations in the density and current field. We next examine how the seasonal variations influence the veering position of the Kuroshio. Using the GEK current data during the years 1953–77, Sun and Su (1994) reported that the Kuroshio at 129°E clearly shows the seasonal meridional migration. According to their report, the Kuroshio veering latitude shifts southward (northward) in summer (winter). The range of migration is about 50 km. This amount appears small but its influence on the regional life and climate is significant. Adopting the same longitude as in their paper, we plot in the top panel of Fig. 16 the seasonal variations of the veering latitude calculated from the NEST3 model. The model result is in good agreement with the observations in both timing and amplitude.

In Fig. 17 we show the vertical section maps along 129°E in the summer and winter seasons. In summer (Fig. 17a), the Kuroshio axis lies south of 30°N and is associated with a strong density stratification. This density stratification is caused by the surface-intensified temperature gradient due to summer heating and also by the low salinity water in the surface layer associated with the large river discharge from Changjiang in summer (Chen et al. 1994). In winter (Fig. 17b), the Kuroshio axis shifts northward by about 0.5° and this shift of the Kuroshio axis coincides with the events of the weakened density gradient, the well-mixed temperature, and the disappearance of the low salinity water in the surface layer. In addition to these local factors, the basin-scale seasonal variation in the heat and salt transports as well as the current itself may also influence the change of stratification there.

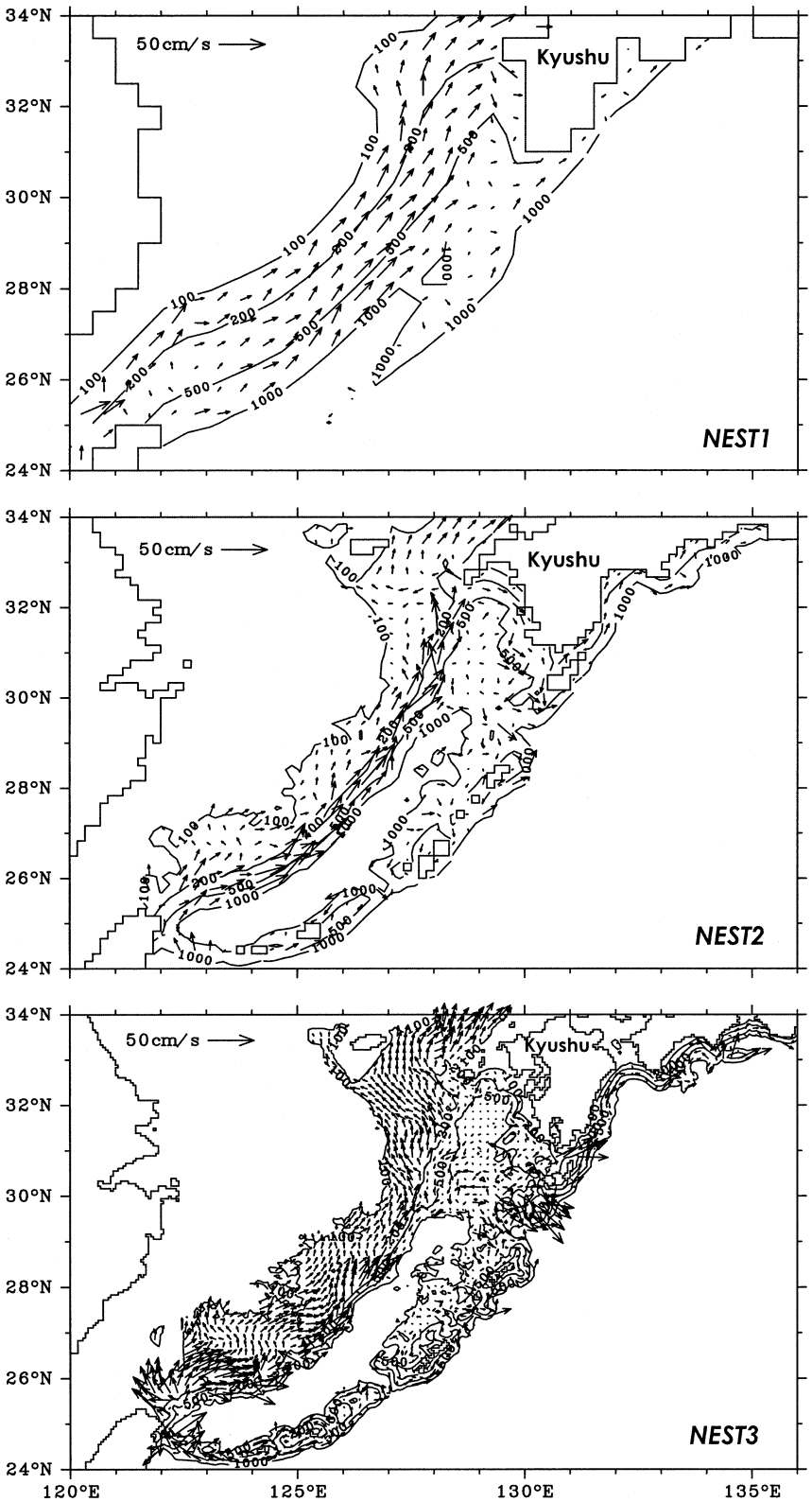

FIG. 14. Mean currents in the bottom sigma layer reproduced by the three models for the same region as in Fig. 10. Note that only the velocity in the region where the depth is between 100 and 1000 m is plotted.

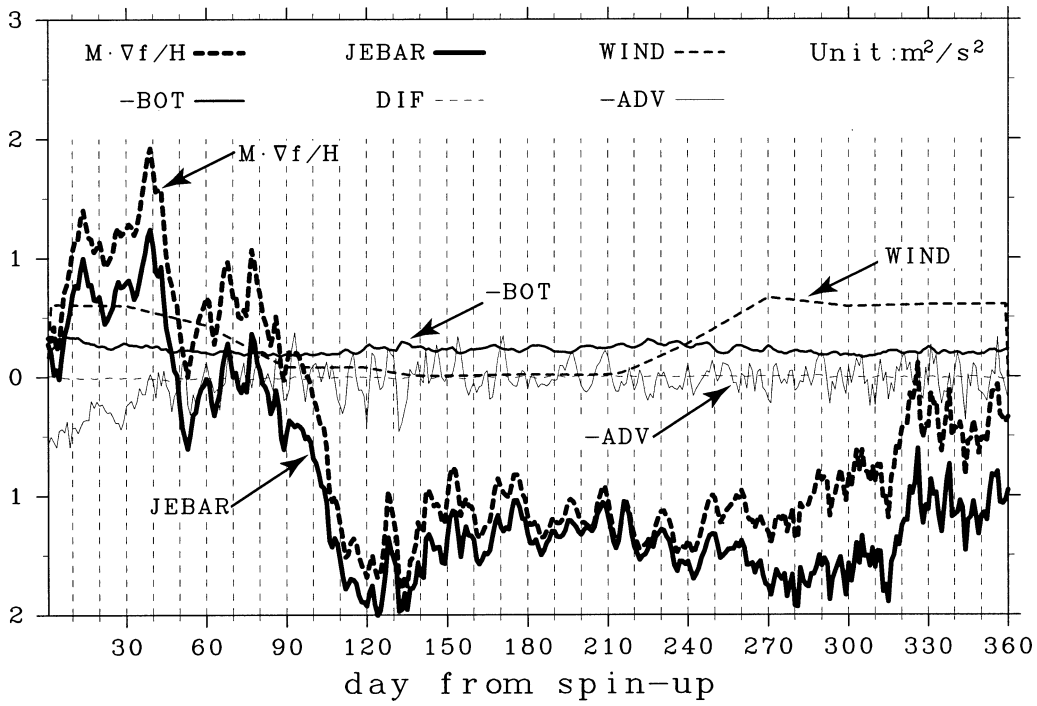

FIG. 15. Temporal variations of six terms in (2) during the early spinup phase of NEST3; shown are the area-integrated values over the box in Fig. 10.

Shown in the bottom panel of Fig. 16 is the seasonal variations of terms in (2) calculated for the same area as in Fig. 15. We see that the summer southward (winter northward) migration of the veering latitude at 129°E is associated with the increase (decrease) of JEBAR. In summer, the stratification is strengthened and the horizontal gradient of density field increases. This leads to increasing the horizontal gradient of potential energy across shelf break and, as a result, the JEBAR effect becomes larger. In winter, the weakened stratification leads to a weaker potential energy gradient across shelf break and thus a weakened JEBAR effect. In this cold season, the role of the wind stress curl as well as the bottom stress curl becomes important and replaces the weakened role of JEBAR.

Before closing this section, we note a close analogy between the seasonal and intermodel migration of the Kuroshio veering position. This analogy is due to the general property of the Kuroshio veering in this section: the more barotropic the Kuroshio becomes, the more northward it migrates.

5. Conclusions

Using a one-way nested system, we developed a model in which three ocean models with different resolution are linked to simulate the Kuroshio in the North Pacific subtropical gyre system. The volume transport through the interface between the coarse and fine model is conserved in an area-integrated sense. The horizontal grid size of each model varies from ½° to 1/18° with the grid ratio of 1/3, but the vertical sigma levels are kept the same for all three models. The three models are all forced by the same wind stress and heat flux data obtained from the nearly real-time satellite observations and bounded by the bottom topography digitized from recently published data: one has a 1/12°-resolution in the Pacific Ocean and the other has a 500-m resolution in the Japanese coastal ocean. Using this triply nested ocean model, we carried out the hindcast experiment for the years 1992–98 starting just after the spinup.

In the first part of the paper, the effect of the model horizontal resolution on the simulated Kuroshio was studied. We have shown that an increase in horizontal resolution greatly affects the path, the current intensity, and the vertical shear associated with the Kuroshio and the variability of sea level, all of which approach the observed features as the model resolution increased. Two factors are found to contribute to this improvement: One is the increased resolution of the model topography, and the other is the improvement of the baroclinic structure of the model Kuroshio. The latter compares well with the observed features with increasing the model resolution.

In general, the coarse-grid model underestimates the baroclinic structure of the Kuroshio. This is because the coarse-grid model cannot reproduce the large horizontal gradient of density field across the Kuroshio. Since the Kuroshio in the ECS is approximately in geostrophic balance, a weaker horizontal density gradient corresponds to a more barotropic nature of the Kuroshio. The

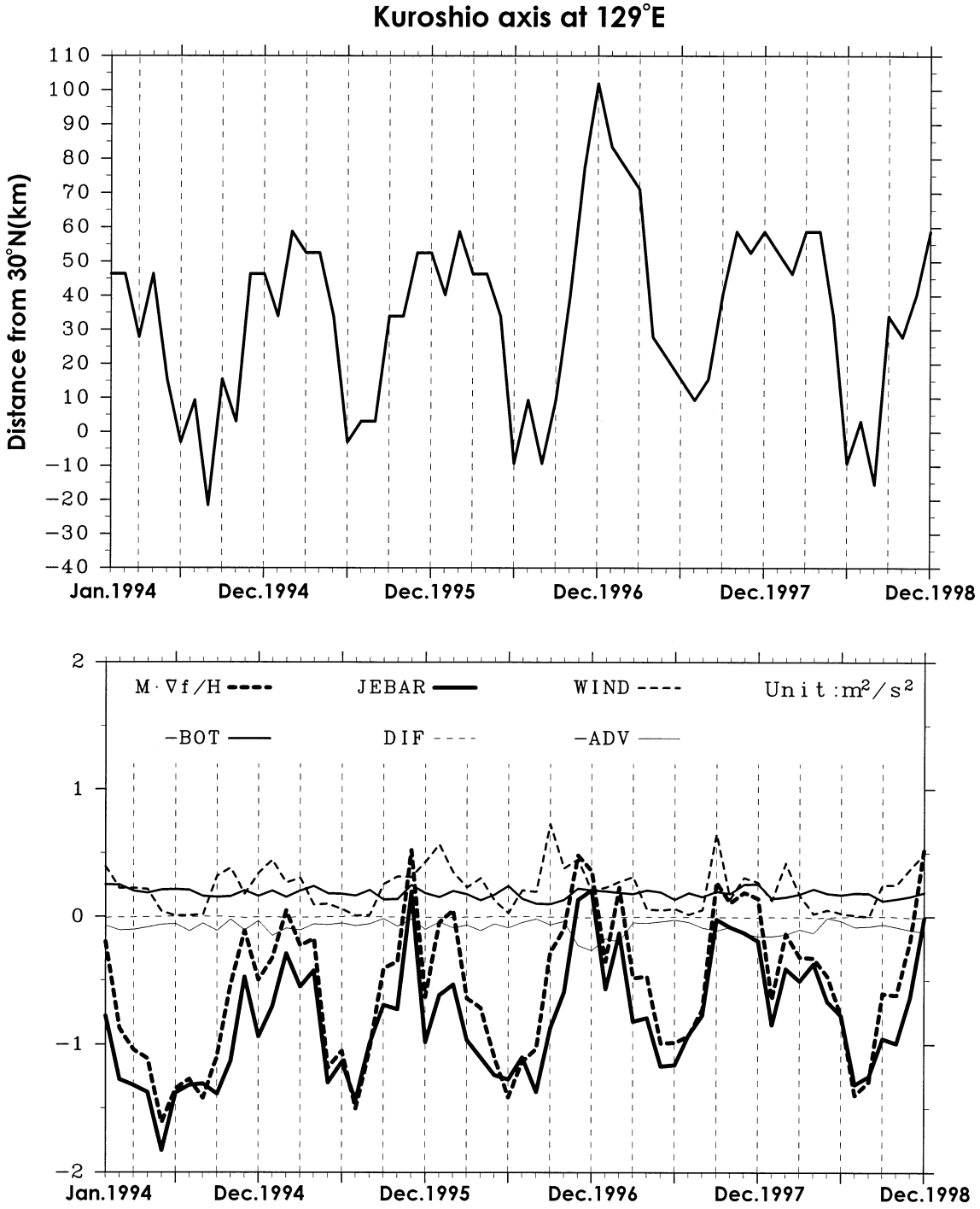

FIG. 16. (top) Seasonal variations of the Kuroshio veering latitude at 129°E; values are monthly averaged ones for the years 1994–98. The Kuroshio axis is defined at the latitude where maximum surface speeds occur (shifts from the mean latitude of the Kuroshio axis at 30°N are measured in kilometers). (bottom) Seasonal variations of six terms in (2); shown are the integrated values over the box in Fig. 10; monthly averaged results from NEST3 hindcast run for the years 1994–98 are used to calculate these terms.

high-resolution model improves this weak baroclinicity of the current by realizing sharp and realistic density fronts across the shelf break. It is worth noting that only the horizontal grid size is changed in our nested model while the vertical resolution is kept the same. Increasing the vertical resolution could directly influence the baroclinic structure. However, with use of a sigma-coordinate model, the refinement of vertical resolution has no effect on the improvement in the bottom topography that plays a crucial role in JEBAR.

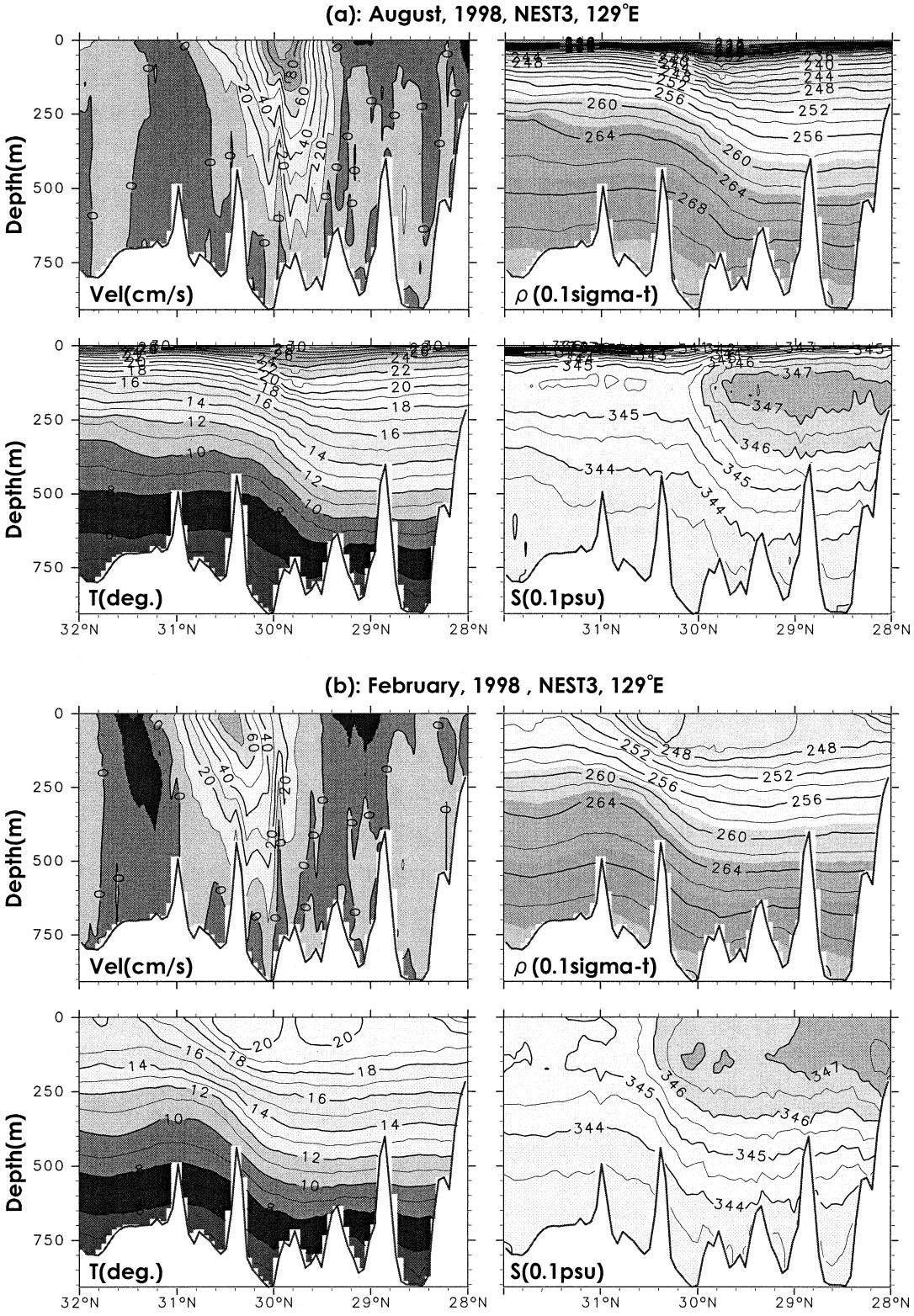

FIG. 17. Vertical section maps at 129°E of the eastward velocity (Vel: cm s^{-1}), density (ρ: 0.1 sigma-*t*), water temperature (T: °C), and salinity (S: 0.1 psu) in (a) Aug 1998 and in (b) Feb 1998; values are monthly averaged over each month and taken from NEST3 results.

The refinement of both topography and baroclinicity in the high-resolution model has naturally led to better representation of the interaction between baroclinicity and topography. We have shown that to resolve this interaction, that is, JEBAR, it is crucial to reproduce the Kuroshio path in the ECS because of the existence of a sharply defined shelf break in the ECS continental shelf/slope region. Tokara Strait is the primary factor that determines where the Kuroshio leaves the ECS. The JEBAR, however, is proved to influence largely the path of the Kuroshio in the ECS. For example, our three models, in which the position of Tokara Strait is the same except for the resolution, reproduced three different paths of the Kuroshio in the ECS.

The NEST3 model reproduced the observed seasonal meridional migration of the Kuroshio path at 129°E. This migration is consistent with the seasonal variation of the JEBAR through seasonal changes of stratification. Interestingly, there is a close analogy between the intermodel difference and the seasonal migration of the Kuroshio veering position. This analogy is due to the mechanism by which the Kuroshio becomes more barotropic and thereby susceptible to topographic control. A coarse (fine) horizontal resolution model tends to yield more barotropic (baroclinic) structure in the model Kuroshio and this structure shifts the Kuroshio veering latitude northward (southward) as in the winter (summer) season when the Kuroshio is more barotropic (baroclinic).

Although the importance of the model horizontal resolution is emphasized in the present article, some problems still remain to be solved. For example, even with the 1/18°-resolution model, we failed to reproduce the short-lived Kuroshio meandering path south of Japan observed, for example, in 1993. One reason for this may be attributed to the failure in reproducing mesoscale eddies south of Honshu, which seem to play an important role in the Kuroshio meandering south of Japan (Ebuchi and Hanawa 2000; Ichikawa 2001; Endoh and Hibiya 2001; Ihara et al. 2001). Resolving the Kuroshio large meander south of Japan in addition to the short-lived meander will be discussed in a subsequent paper (Y. Miyazawa, X. Guo, and T. Yamagata 2002, unpublished manuscript).

Acknowledgments. This work is a part of J-COPE (Japanese Coastal Ocean Predictability Experiment) of FRSGC, which is supported by National Space Development Agency and Japan Marine Science and Technology Center. We also acknowledge the kind support from IOC/UNESCO NEAR-GOOS project (Chairperson Prof. K. Taira). Discussions with Drs. T. Kagimoto, S. Minato, and H. Sakuma were very helpful in the model development. We also thank Dr. E. Oka for kindly providing the figure of observation data at PN line. Several comments of anonymous reviewers helped to improve the original manuscript.

APPENDIX

Adjustment of Volume Transport through the Interface between the Fine and Coarse Grid Model

In this appendix we consider how the one-way nested model can conserve the volume over the nested area. Let us consider the continuity equation,

$$\frac{\partial \eta}{\partial t} = -\nabla \cdot [(H + \eta)\mathbf{u}], \tag{A1}$$

where η, H, and $\mathbf{u}$ are the elevation, depth, and vertical-averaged velocity vector, respectively. Integrating (A1) over the nested area yields

$$\frac{\partial}{\partial t}\left(\int\int \eta \, dx \, dy\right) = T_N + T_S + T_W + T_E, \tag{A2}$$

where

$$T_N\left\{= -\int_W^E [(H + \eta)v]_N \, dx\right\},$$

$$T_S\left\{= \int_W^E [(H + \eta)v]_S \, dx\right\},$$

$$T_W\left\{= \int_S^N [(H + \eta)u]_W \, dx\right\}, \quad \text{and}$$

$$T_E\left\{= -\int_S^N [(H + \eta)u]_E \, dx\right\}$$

represent the transport (taken positive inward) across the northern, southern, western, and eastern nested boundaries, respectively. Now, in order to conserve the volume between the fine and coarse grid models, it is necessary to satisfy the following relation:

$$\frac{\partial}{\partial t}\left(\int\int \eta_f \, dx \, dy\right) = \frac{\partial}{\partial t}\left(\int\int \eta_c \, dx \, dy\right), \tag{A3}$$

where η_f and η_c are the elevation of the fine and coarse grid models, respectively, and the surface integral is taken over the nested area. Now, a deficit in the transport of the fine grid model, δT, is given by

$$\delta T = (T_{N,c} + T_{S,c} + T_{W,c} + T_{E,c}) - (T_{N,f} + T_{S,f} + T_{W,f} + T_{E,f}), \tag{A4}$$

where the subscripts f and c refer to the fine and coarse grid model, respectively. The total transect area of the fine grid model along the nested boundary is given by

$$S_f = \sum (H_f + \eta_f)\delta l, \tag{A5}$$

where δl is the grid interval of the fine mesh. Define the average of the transport deficit by

$$\delta u = \delta T / S_f. \tag{A6}$$

The corrected normal component of the fine grid model external velocity is thus

$$v^*_{N,f} = v_{N,f} - \delta u$$
$$v^*_{S,f} = v_{S,f} + \delta u$$
$$u^*_{W,f} = u_{W,f} + \delta u$$
$$u^*_{E,f} = u_{E,f} - \delta u. \quad \text{(A7)}$$

The plus (or minus) sign in (A7) means that the averaged deficit in the transport (i.e., $|\delta u|$) should be subtracted from the normal velocity on the northern and eastern sides, but added to the normal velocity on the southern and western sides. It is easily shown that (A7) satisfies

$$T^*_f = T_f + (T_c - T_f) = T_c. \quad \text{(A8)}$$

Thus the velocity defined by (A7) can satisfy the volume conservation equation, (A3).

As shown in Fig. 4, each model gives very similar distributions and amplitudes of sea level. This suggests that the volume transport through each model interface is conserved well and the simple adjustment of the normal flux as expressed by (A7) works quite well.

Furthermore, although the above correction is enough to give the volume conservation for our nested model, this does not necessarily means that the sea level is locally continuous across the nested boundary. The final value of the normal external velocity at the fine-mesh boundary is thus given by the value as corrected in (A7) plus a flux toward the outside (or inside) of the boundary, whose value is proportional to the sea level difference between two grids on opposite sides of the boundary with a proportionality constant equal to $0.1\sqrt{g/H}$, where g is the gravitational acceleration. This local adjustment of the normal component of the external mode velocity is necessary for a smooth continuous sea level across the nested boundary, as used in subroutine BCOND of the POM.

REFERENCES

Barnier, B., 1998: Forcing the ocean. *Ocean Modeling and Parameterization,* E. P. Chassignet and J. Verron, Eds., Kluwer Academic, 45–80.

Blumberg, A. F., and G. L. Mellor, 1987: A description of a three-dimensional coastal ocean circulation model. *Three-Dimensional Coastal Ocean Models,* N. Heaps, Ed., Coastal and Estuarine Series, No. 4, Amer. Geophys. Union, 1–16.

Chen, C., R. C. Beardsley, R. Limeburner, and K. Kim, 1994: Comparison of winter and summer hydrographic observations in the Yellow and East China Seas and adjacent Kuroshio during 1986. *Cont. Shelf Res.,* **14,** 909–929.

da Silva, A. M., C. C. Young-Molling, and S. Levitus, 1994: *Algorithms and Procedures.* Vol. 1, *Atlas of Surface Marine Data 1994,* NOAA Atlas NESDIS 6, 83 pp.

Ebuchi, N., and K. Hanawa, 2000: Mesoscale eddies observed by TOLEX-ADCP and TOPEX/POSEIDON altimeter in the Kuroshio recirculation region south of Japan. *J. Oceanogr.,* **56,** 43–57.

Emery, W. J., and R. E. Thomson, 1998: *Data Analysis Methods in Physical Oceanography.* Pergamon, 634 pp.

Endoh, T., and T. Hibiya, 2001: Numerical simulation of the transient response of the Kuroshio leading to the large meander formation south of Japan. *J. Geophys. Res.,* **106,** 26 833–26 850.

Ezer, T., and G. L. Mellor, 1997: Simulations of the Atlantic Ocean with a free surface sigma coordinate ocean model. *J. Geophys. Res.,* **102,** 15 647–15 657.

Geophysical Exploration Technology (GETECH), 1995: Global DTM5, 5′ × 5′ digital terrain model of the world. University of Leeds Innovations, CD-ROM.

Greatbatch, R. J., and A. Goulding, 1990: On the seasonal variation of transport through the Tokara Strait. *J. Oceanogr. Soc. Japan,* **46,** 9–20.

Hellerman, S., and M. Rosenstein, 1983: Normal monthly wind stress over the world ocean with error estimates. *J. Phys. Oceanogr.,* **13,** 1093–1104.

Hinada, T., 1996: Seasonal variation and long-term trends of the oceanographic conditions along a fixed hydrographic line crossing the Kuroshio in the East China Sea. *Oceanogr. Mag.,* **45,** 9–32.

Hukuda, H., A. E. Hay, and R. J. Greatbatch, 2001: A two-layer model of shelf break jets with application to the Labrador Current. *J. Phys. Oceanogr.,* **31,** 324–335.

Ichikawa, K., 2001: Variation of the Kuroshio in the Tokara Strait induced by mesoscale eddies. *J. Oceanogr.,* **57,** 55–68.

Ihara, C., T. Kagimoto, Y. Masumoto, and T. Yamagata, 2001: Eddy formation near the Izu-Ogasawara Ridge and its link with seasonal adjustment of subtropical gyre in the Pacific. *Extended Abstracts, 11th PAMS/JECSS Workshop,* Cheju, Korea, 9–10.

Kagimoto, T., and T. Yamagata, 1997: Seasonal transport variations of the Kuroshio: An OGCM simulation. *J. Phys. Oceanogr.,* **27,** 403–418.

Kubota, M., H. Yokota, and T. Okamoto, 1995: Mechanism of the seasonal transport variation through Tokara Strait. *J. Oceanogr.,* **51,** 441–458.

Levitus, S., and T. P. Boyer, 1994: *Temperature.* Vol. 4, *World Ocean Atlas 1994,* NOAA Atlas NESDIS 4, 117 pp.

——, R. Burgett, and T. P. Boyer, 1994: *Salinity.* Vol. 3, *World Ocean Atlas 1994,* NOAA Atlas NESDIS 3, 99 pp.

Mellor, G. L., 1998: User's guide for a three-dimensional, primitive equation, numerical ocean model. Rep., Program in Atmospheric and Oceanic Science, Princeton University, 41 pp.

——, T. Ezer, and L.-Y. Oey, 1994: The pressure gradient conundrum of sigma coordinate ocean models. *J. Atmos. Oceanic Technol.,* **11,** 1126–1134.

Nitani, H., 1972: Beginning of the Kuroshio. *The Kuroshio—Its Physical Aspects,* H. Stommel and K. Yoshida, Eds., University of Tokyo Press, 129–163.

Oka, E., and M. Kawabe, 1998: Characteristics of variations of water properties and density structure around the Kuroshio in the East China Sea. *J. Oceanogr.,* **54,** 605–617.

Qiu, B., and N. Imasato, 1990: A numerical study on the formation of the Kuroshio Counter Current and the Kuroshio Branch Current in the East China Sea. *Cont. Shelf Res.,* **10,** 165–184.

Reynolds, R. W., and T. M. Smith, 1994: Improved global sea surface temperature analyses. *J. Climate,* **7,** 929–948.

Sekine, Y., and K. Kutsuwada, 1994: Seasonal variation in volume transport of the Kuroshio south of Japan. *J. Phys. Oceanogr.,* **24,** 261–272.

Smith, R. D., M. E. Maltrud, F. O. Bryan, and M. W. Hecht, 2000: Numerical simulation of the north Atlantic Ocean at 1/10°. *J. Phys. Oceanogr.,* **30,** 1532–1561.

Spall, M. A., and W. R. Holland, 1991: A nested primitive equation model for oceanic applications. *J. Phys. Oceanogr.,* **21,** 205–220.

Sun, X.-P., and Y.-F. Su, 1994: On the variation of Kuroshio in East China Sea. *Oceanology of China Seas,* Vol. 1, D. Zhou, Y.-B. Liang, and C. K. Tseng, Eds., Kluwer Academic 49–58.

Warren, B. A., 1963: Topographic influences on the path of the Gulf Stream. *Tellus,* **15,** 167–183.

Yuan, Y., J. Su, Z. Pan, H. Chen, G. Ichikawa, S. Imawaki, K. Kawatabe, K. Takano, and S. Umatani, 1995: The western boundary current east of the Ryukyu Islands. *La Mer,* **33,** 1–11.